

Figure 1

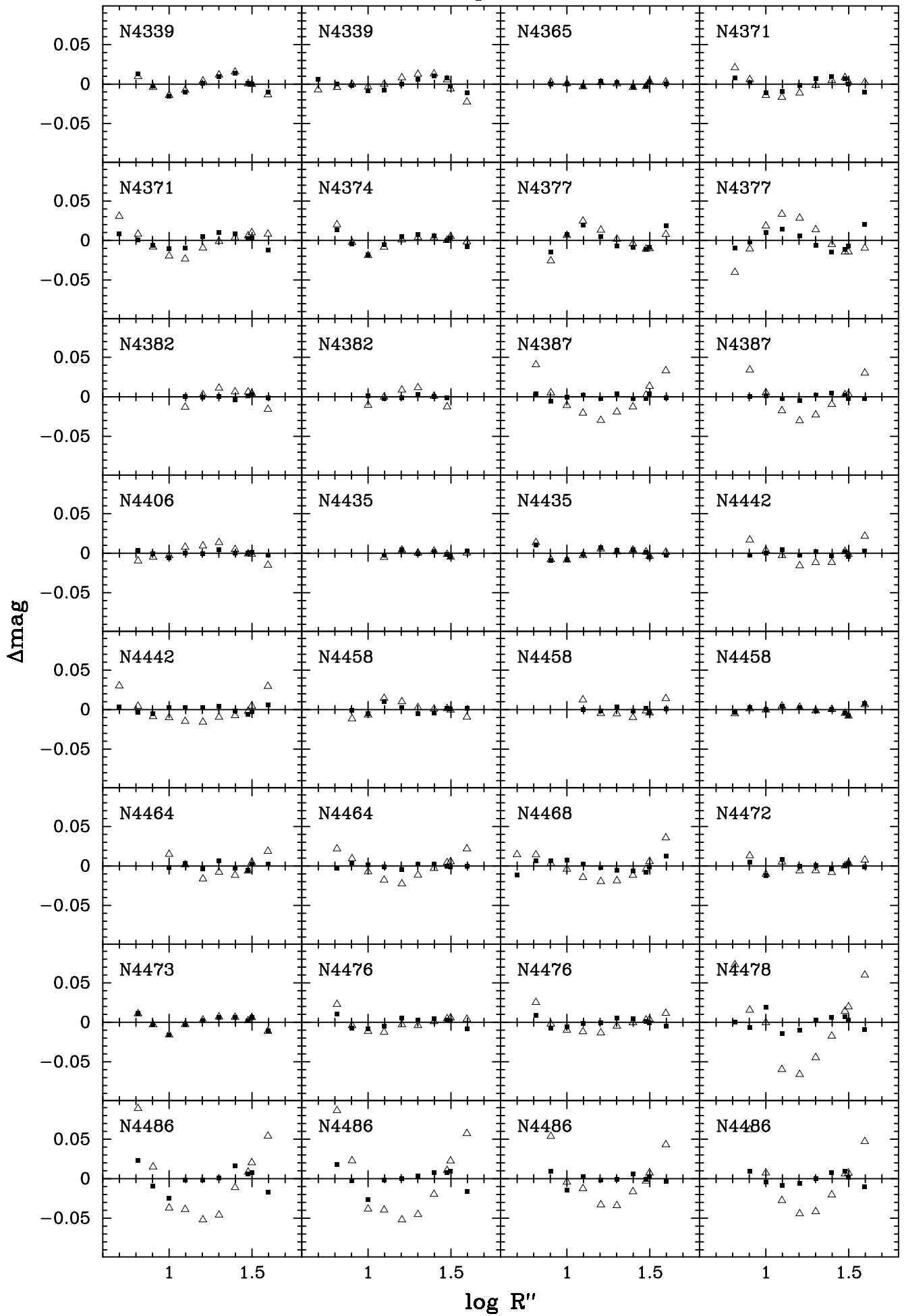


Figure 1

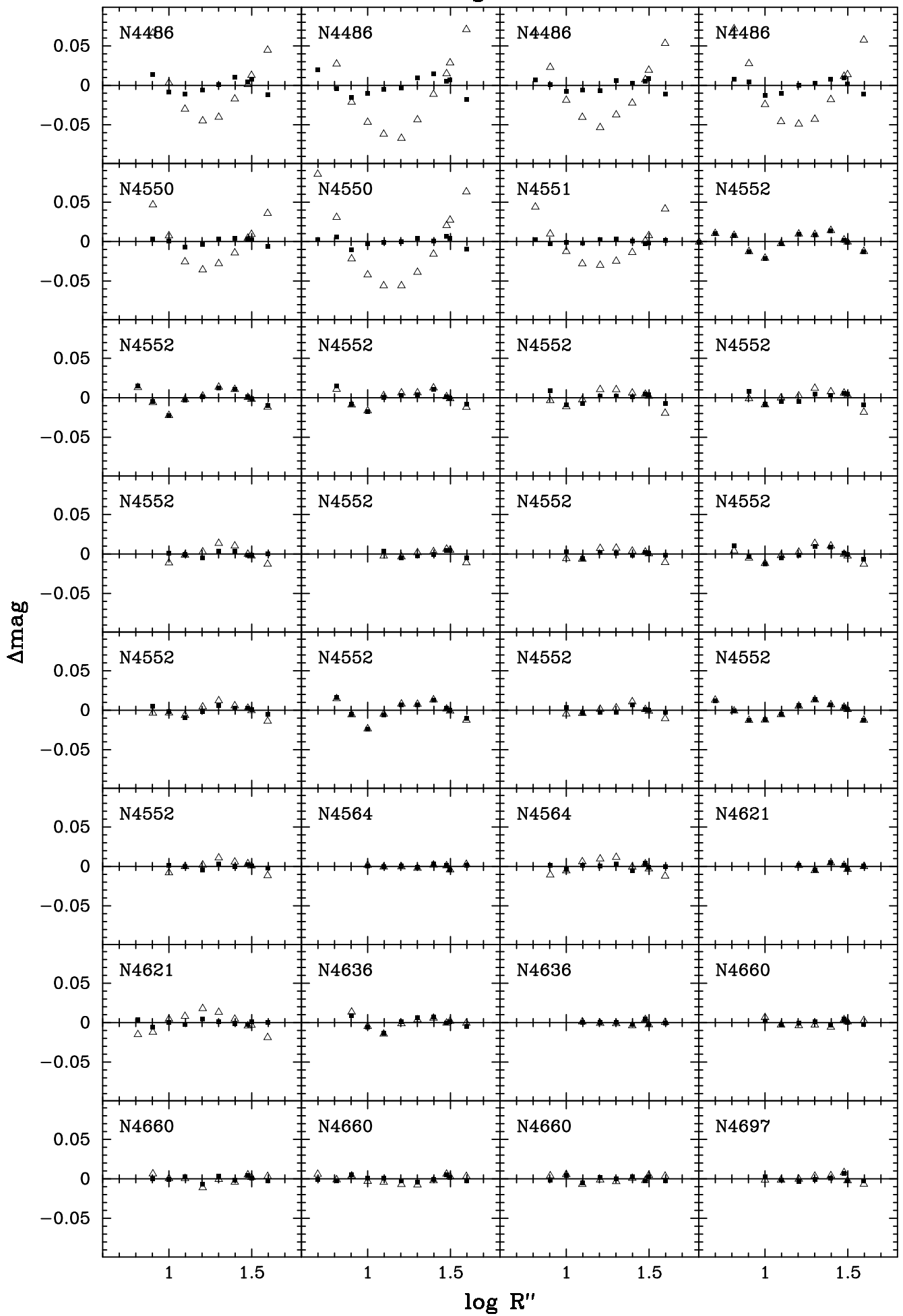


Figure A1

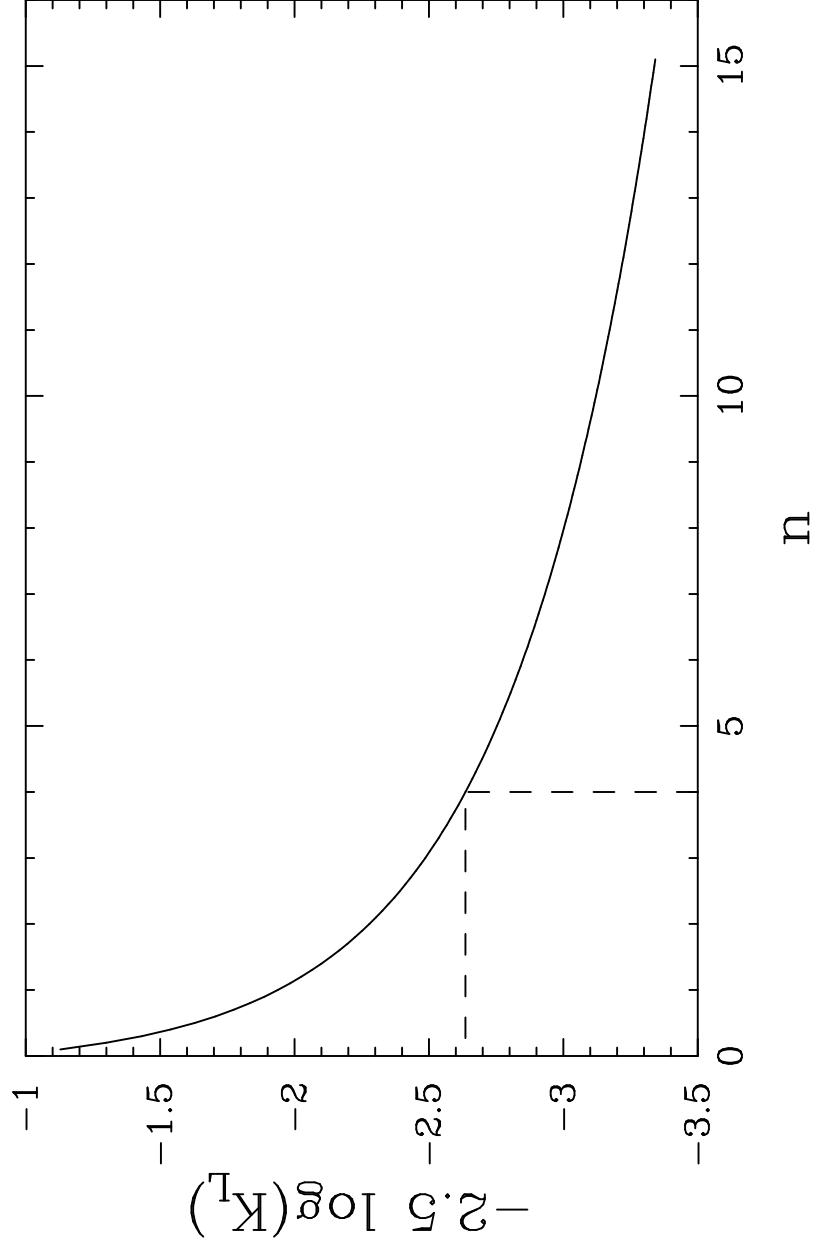


Figure B1

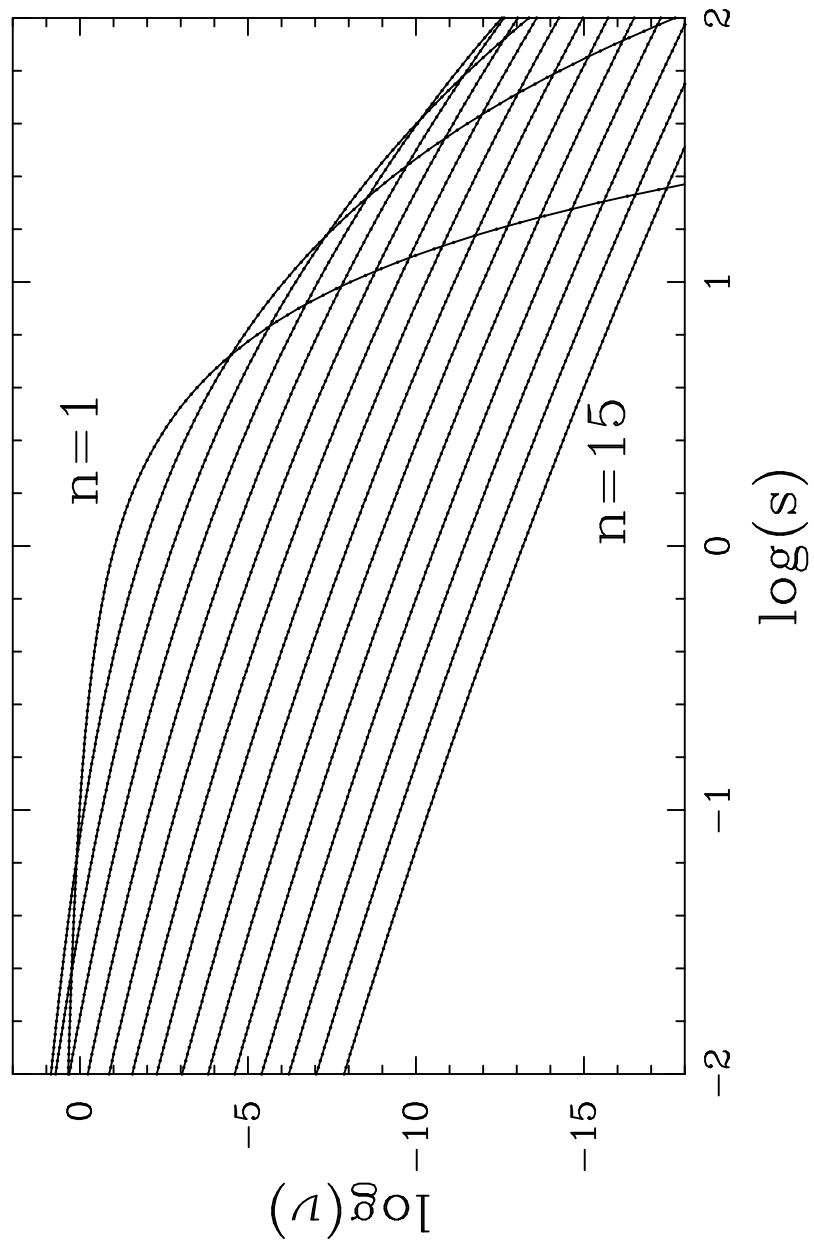


Figure 2

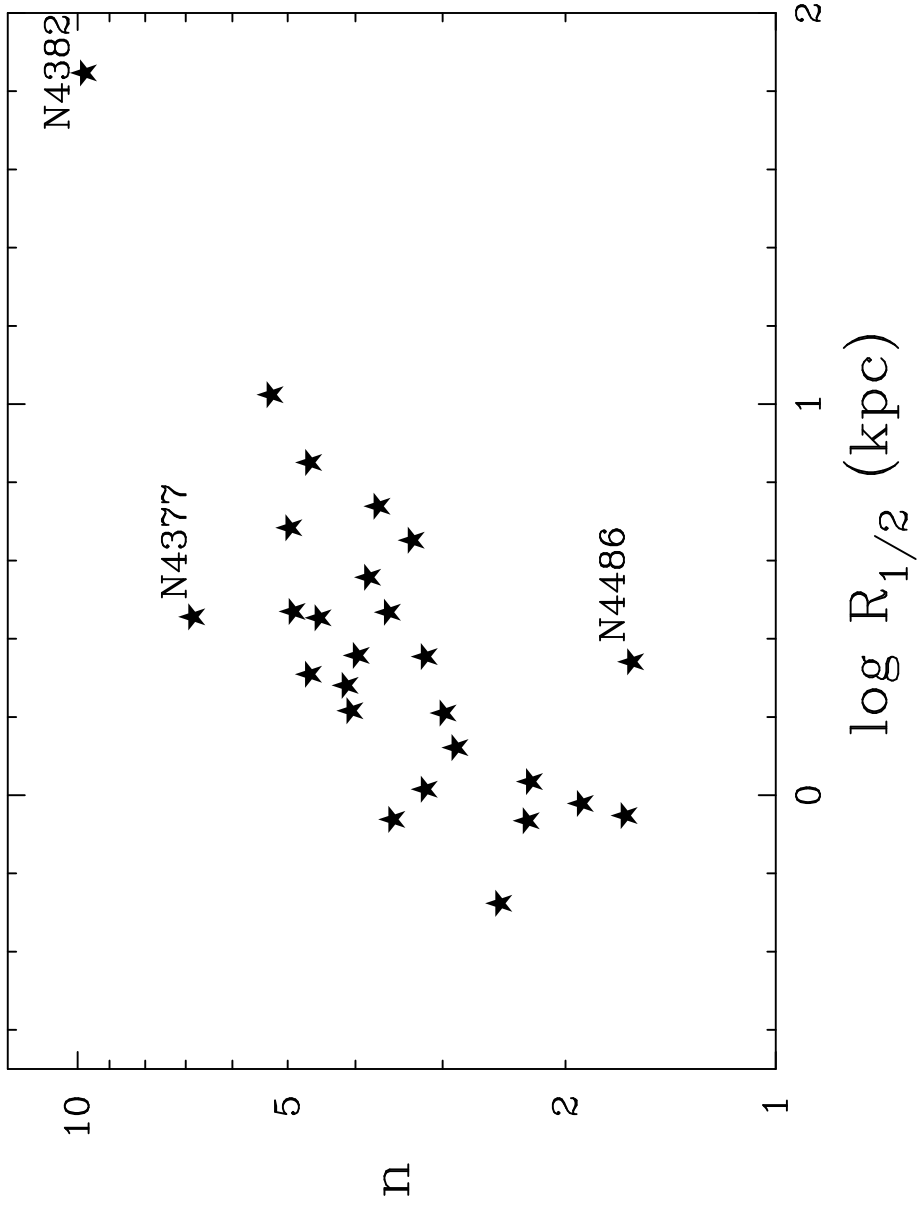


Figure B2

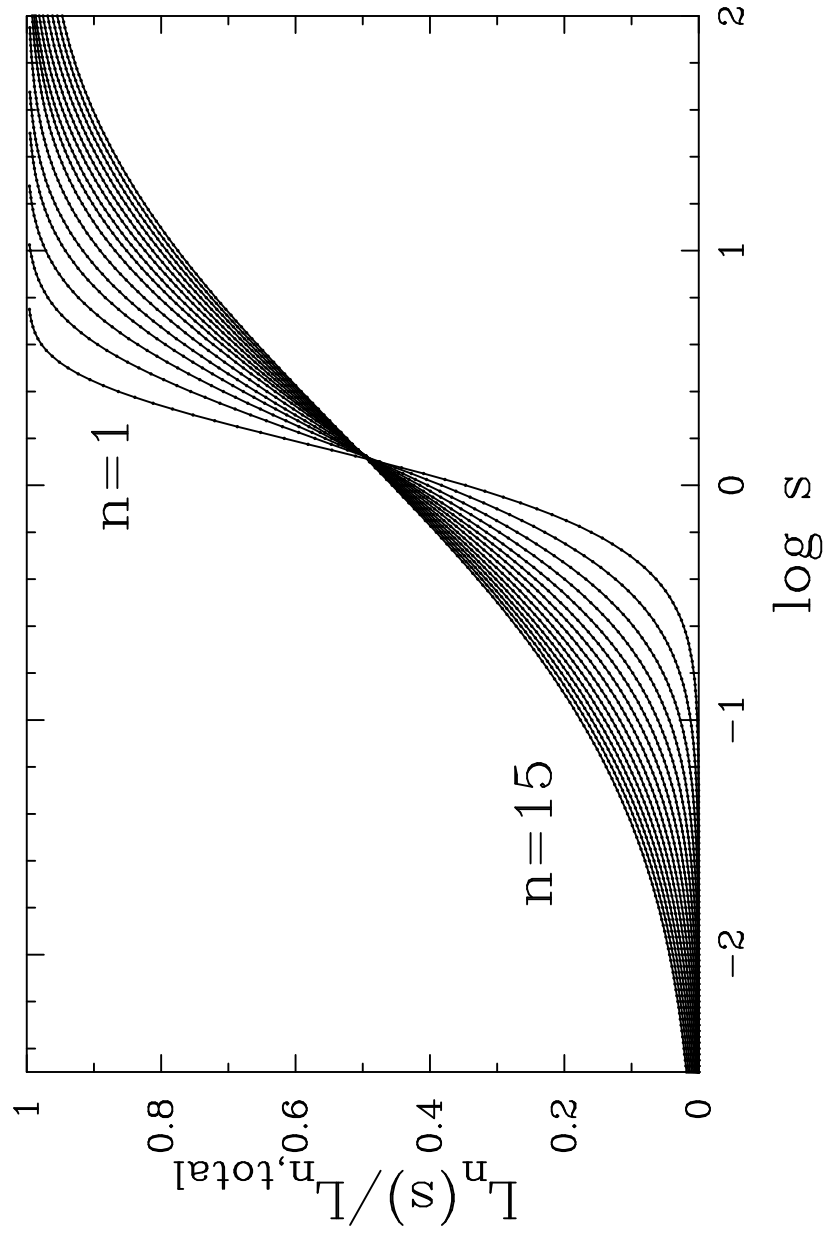


Figure 3

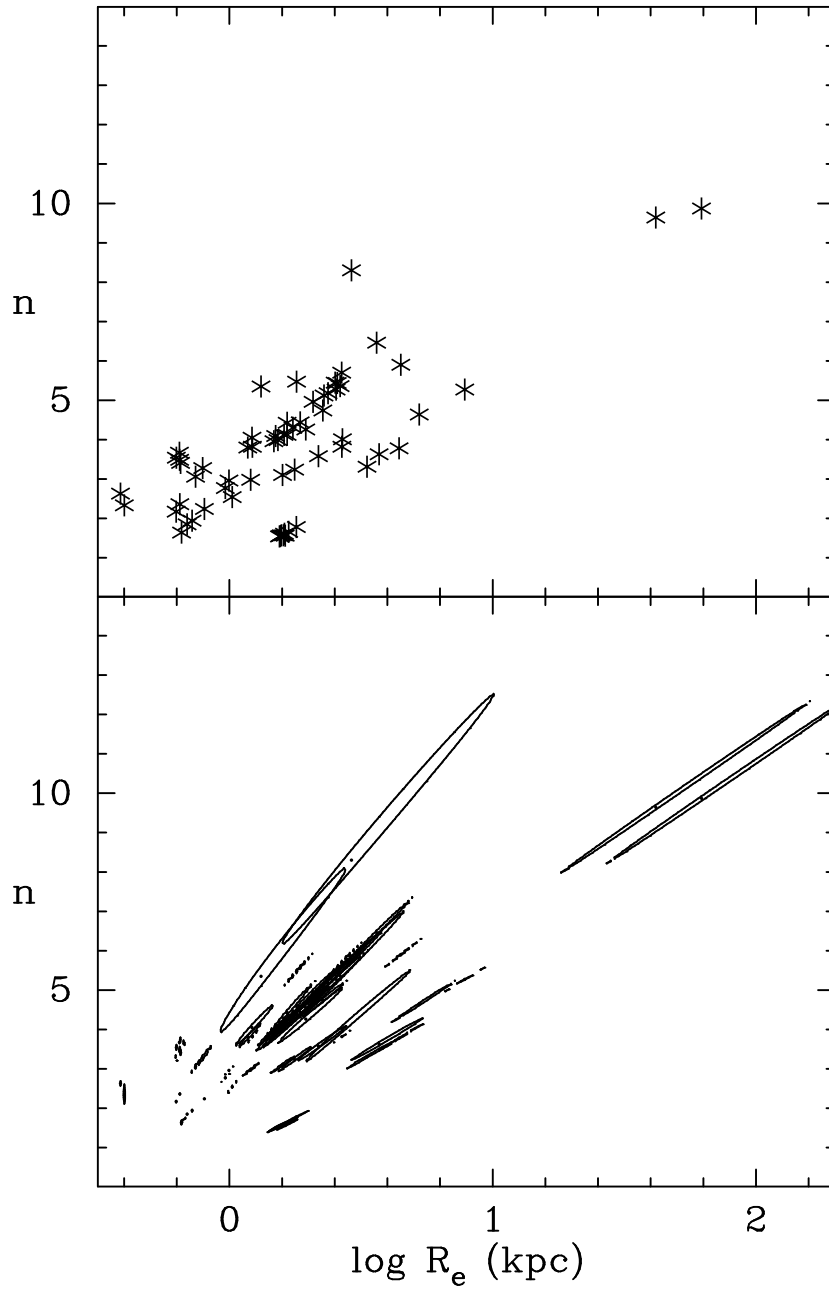


Figure 4

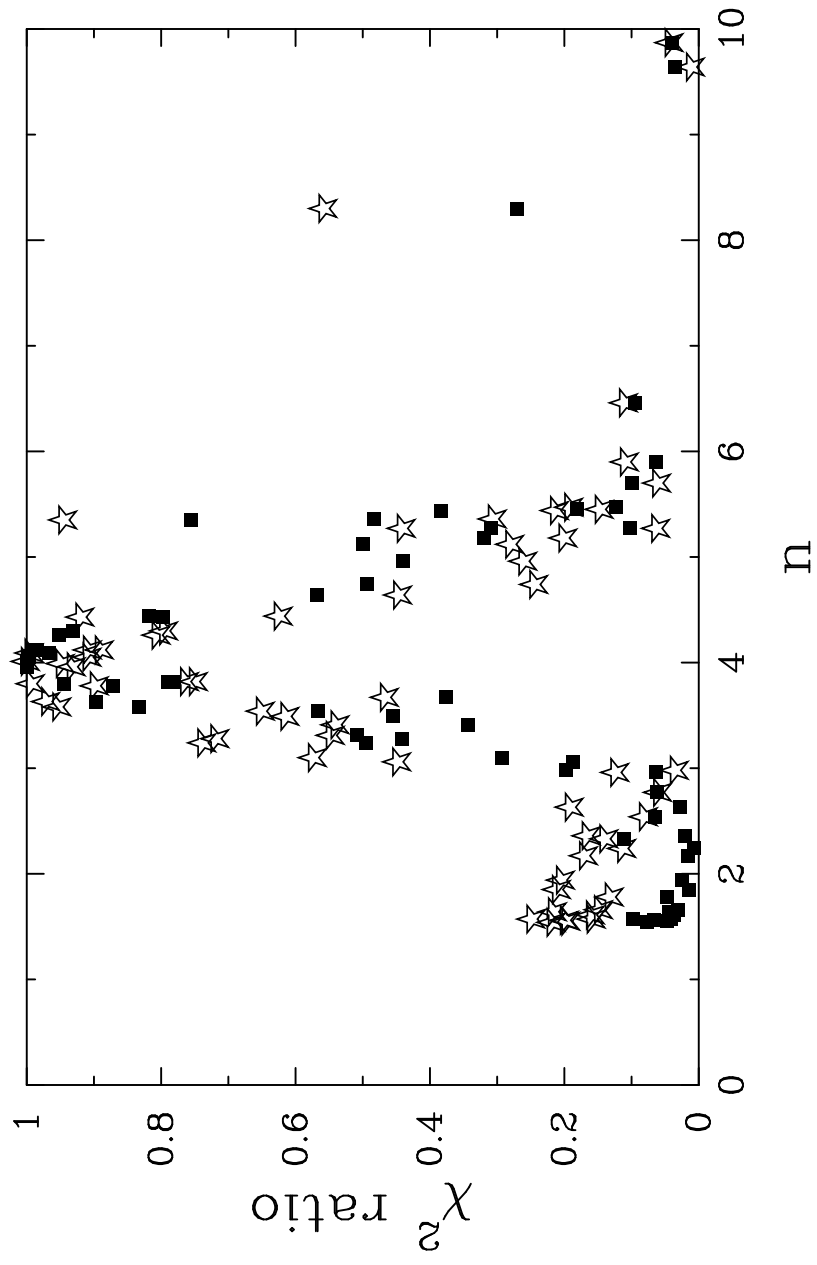


Figure 5

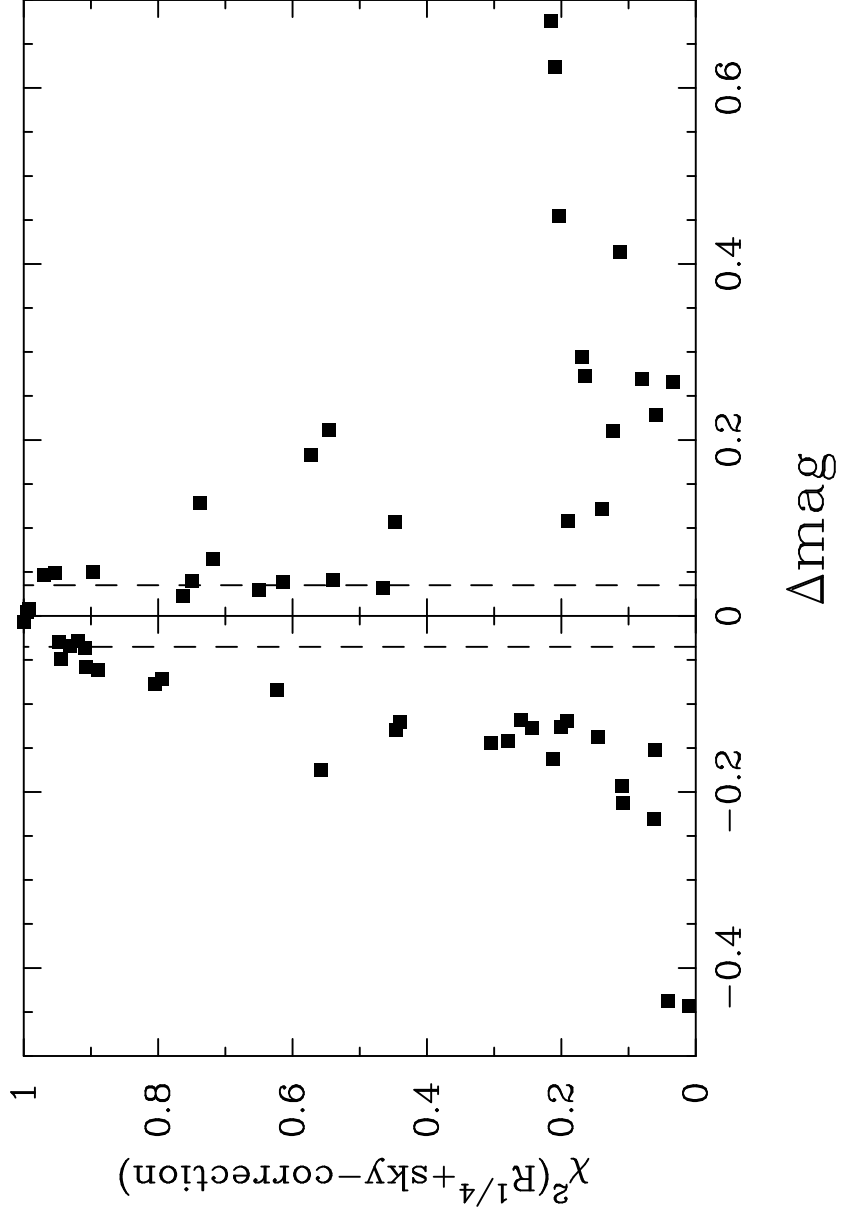


Figure 6

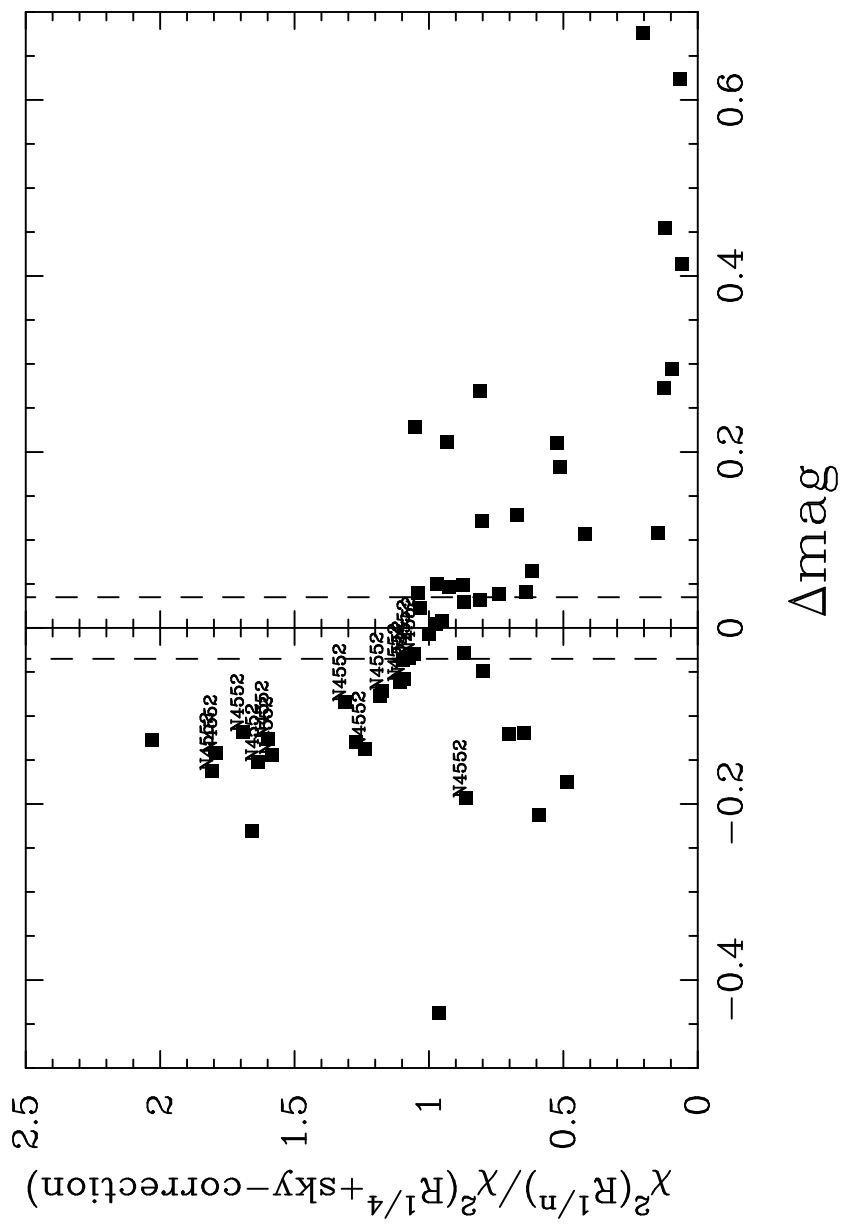


Figure 7

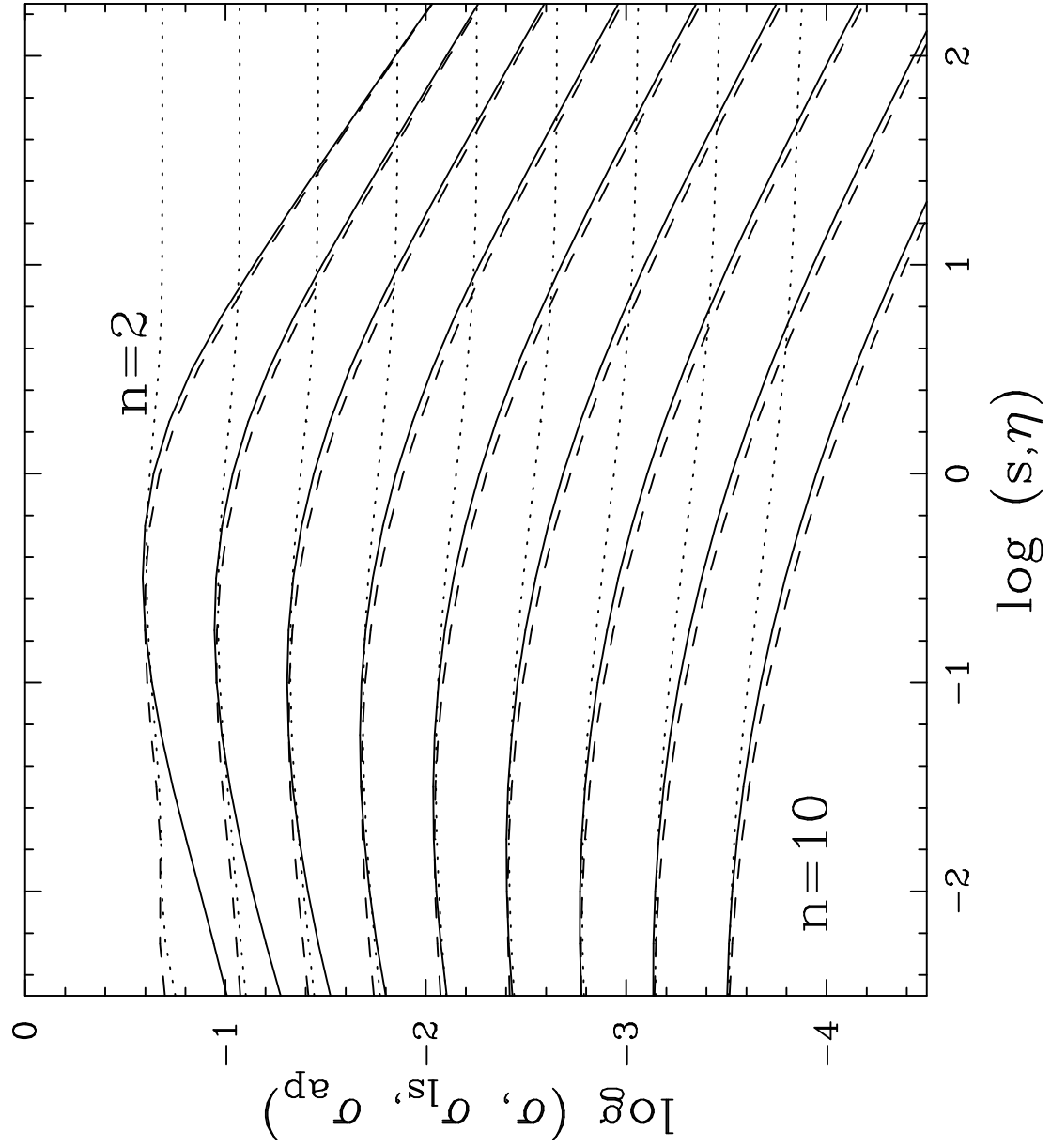


Figure 8

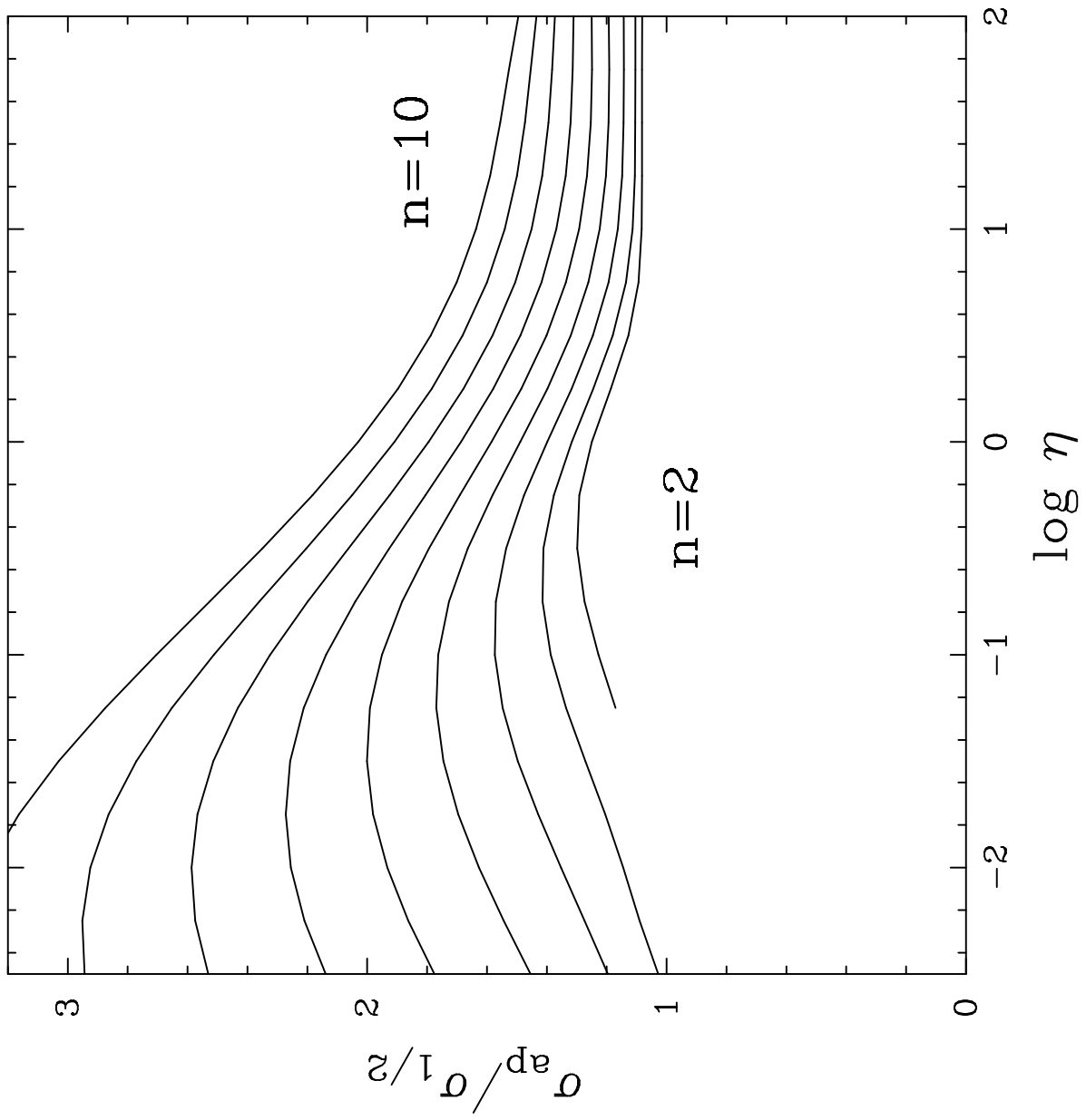


Figure 9

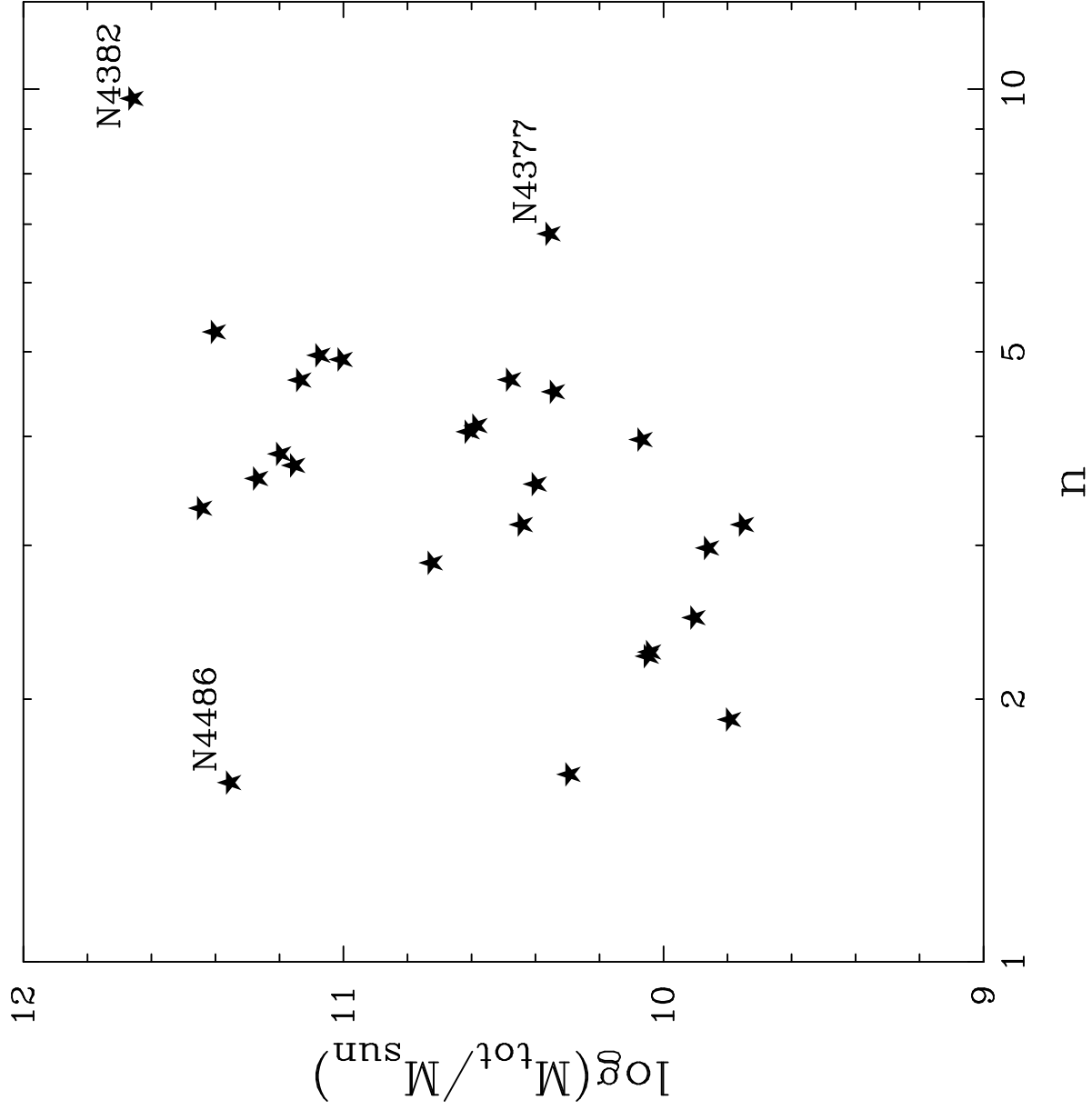


Figure 10

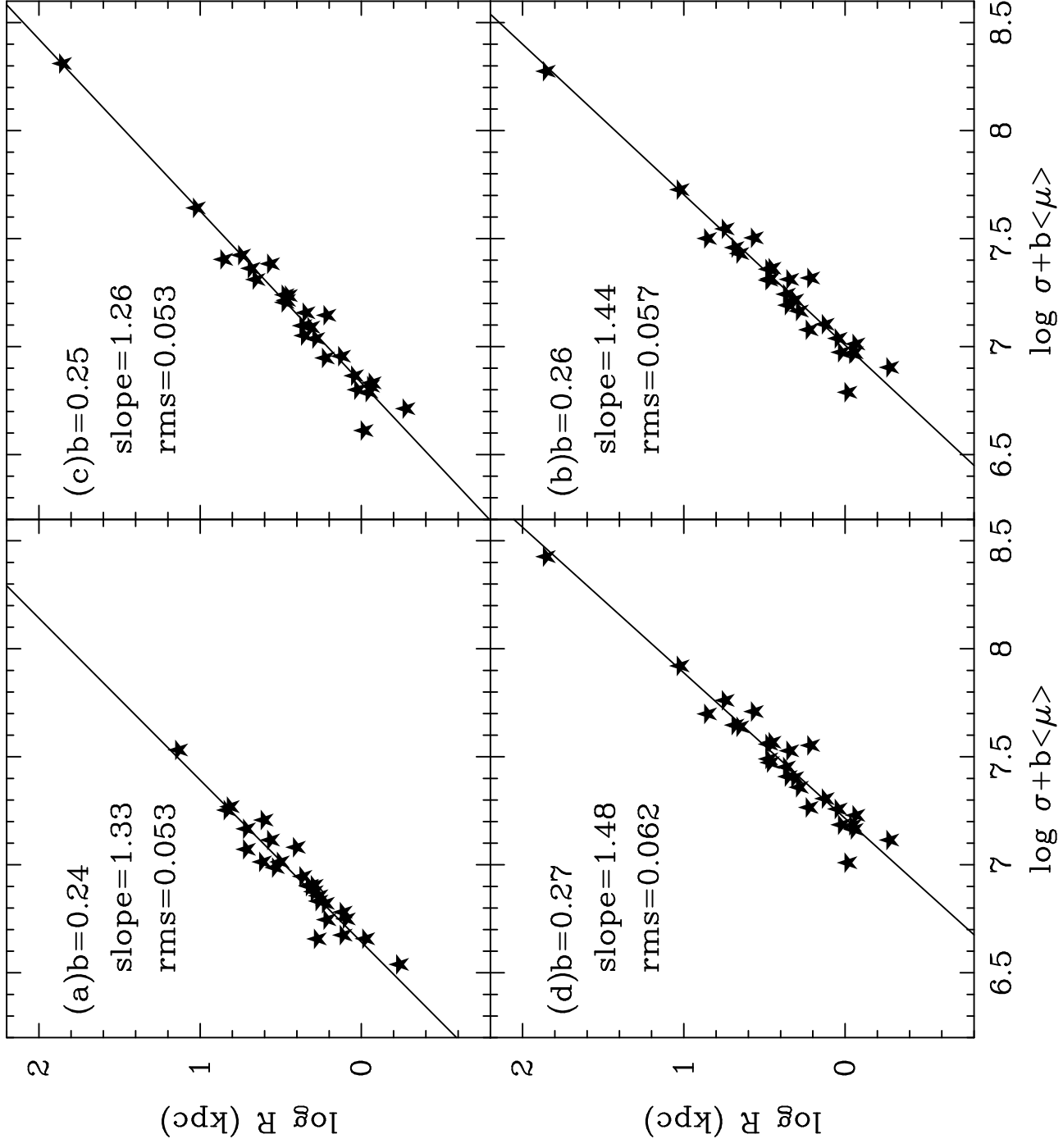
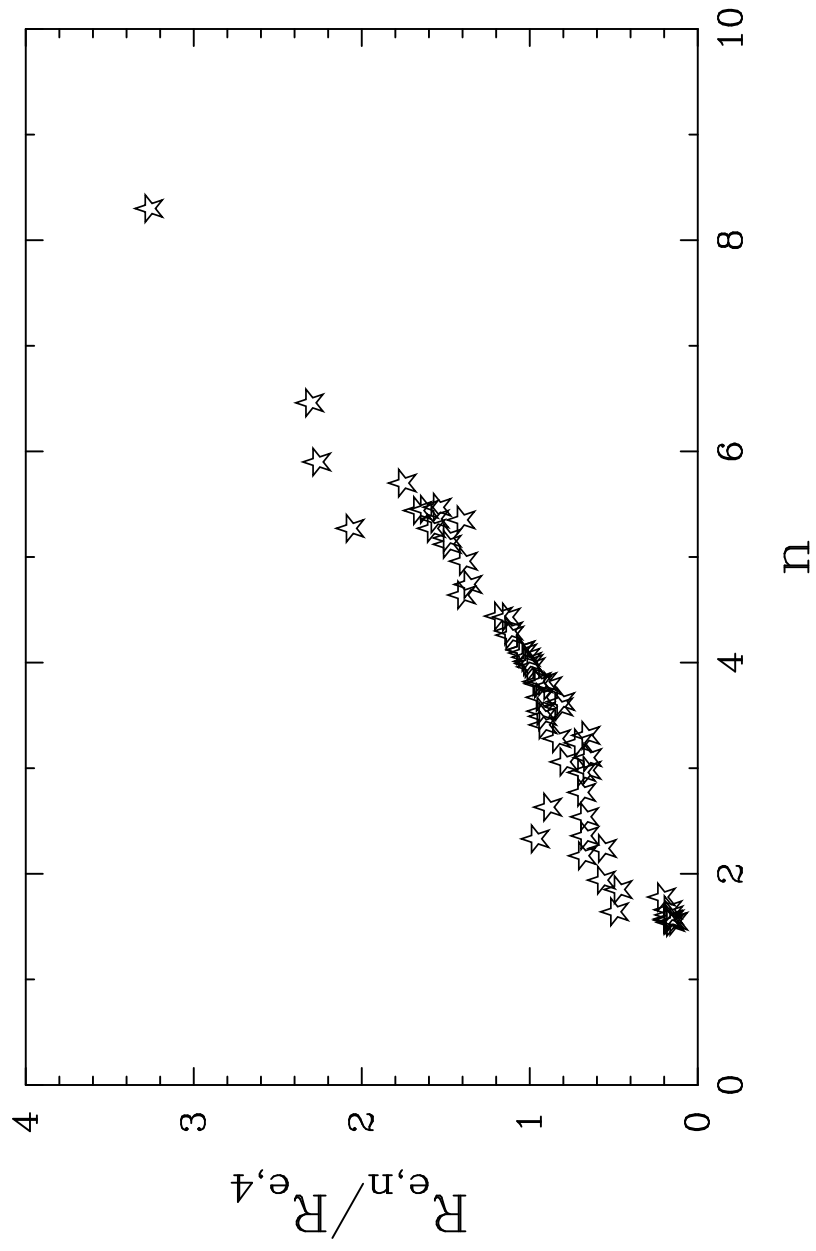


Figure 11



Some Effects of Galaxy Structure and Dynamics on the Fundamental Plane

Alister Graham^{*} and Matthew Colless^{*}

*Mount Stromlo and Siding Spring Observatories, The Australian National University,
Private Bag, Weston Creek PO, ACT 2611, Australia.*

ABSTRACT

We examine the effects on the Fundamental Plane (FP) of structural departures from an $R^{1/4}$ galaxy light profile. We also explore the use of spatial (i.e. volumetric) as well as projected galaxy parameters. We fit the Sersic $R^{1/n}$ law to the V-band light profiles of 26 E/S0 Virgo galaxies, where n is a shape parameter that allows for structural differences amongst the profiles. The galaxy light profiles show a trend of systematic departures from a de Vaucouleurs $R^{1/4}$ law, in the sense that n increases with increasing effective half-light radius R_e . This results in R_e , and the associated mean surface brightness within this radius, having systematic biases when constructed using an $R^{1/4}$ law. Adjustments to the measured velocity dispersion are also made, based upon the theoretical velocity dispersion profile shapes of the different $R^{1/n}$ light profiles, constructed assuming spherical symmetry and isotropic pressure support.

We construct the FP for the case when structural homology is assumed (specifically, an $R^{1/4}$ law is fitted to all galaxies) and central velocity dispersions, σ_0 , are used. The plane we obtain is $R_e \propto \sigma_0^{1.33 \pm 0.10} \Sigma_e^{-0.79 \pm 0.11}$, where Σ_e is the mean surface brightness within the projected effective radius R_e . This agrees with the FP obtained by others and departs from the virial theorem expectation $R \propto \sigma^2 \Sigma^{-1}$. We find that allowing for broken structural homology through fitting $R^{1/n}$ profiles (with n a free parameter), but still using central velocity dispersions, actually increases the departure of the observed FP from the virial plane — the increase in effective radius with galaxy luminosity (and n) is over-balanced by an associated decrease in the mean surface brightness.

In examining the use of spatial quantities and allowing for the different velocity dispersion profiles corresponding to the observed light profiles, we find that use of the spatial velocity dispersion at the spatial half-light radius decreased the departure of the observed FP from the virial plane. (Use of the spatial half-light radius and mean surface brightness term had no effect on the FP as they are constant multiples of their projected values). Through use of the Jeans hydrodynamical equation, we convert the projected central aperture velocity dispersion, σ_0 , into the infinite aperture velocity dispersion, $\sigma_{\text{tot},n}$ (which is equal to one-third of the virial velocity dispersion). Using both the $R^{1/n}$ fit and $\sigma_{\text{tot},n}$ we obtain $R_{e,n} \propto \sigma_{\text{tot},n}^{1.44 \pm 0.11} \Sigma_{e,n}^{-0.93 \pm 0.08}$. Making the fullest allowance for broken structural homology thus brings the observed FP closer to the virial plane, with the exponent of the surface brightness term consistent with the virial expectation.

Key words: galaxies: fundamental parameters – galaxies: structure – galaxies: elliptical and lenticular, cD – galaxies: dark matter – galaxies: kinematics and dynamics.

1 INTRODUCTION

It has been known for some years that elliptical galaxies are well represented by a two dimensional surface in the space defined by their observable parameters (Brosche & Lenters

^{*} E-mail: ali@mso.anu.edu.au; colless@mso.anu.edu.au

1983; Djorgovski 1987a; Lynden-Bell et al. 1988a). This two dimensional manifold, commonly shown in the logarithmic 3-space of radius (R_e), intensity (I_e), and central velocity dispersion (σ_0), has come to be known as the Fundamental Plane (FP) (Djorgovski & Davis 1987; Dressler et al. 1987b). The existence of such a plane has implications for the formation and evolutionary processes of elliptical galaxies. Furthermore, the small scatter about the FP makes it a useful tool for estimating distances to elliptical galaxies. Acknowledging some degree of scatter about the FP, either intrinsic to the galaxies and/or due to measurement errors, the deviations from the FP have been interpreted as peculiar velocities (Dressler et al. 1987a; Dressler & Faber 1990). For such methods of studying peculiar velocity fields and bulk flow motions, the exact FP used is a crucial factor.

Under the assumptions of kinematic and structural homology (i.e. identical form and shape for the kinematic and density profiles) amongst galaxies, the virial theorem predicts that galaxies will occupy a plane in log-space amongst the observables radius (R_e), mass surface density (η_e), and central velocity dispersion (σ_0) (Faber et al. 1987). The transformation between this plane and the observed plane is given by the mass-to-light ratios, M/L , of the galaxies. Furthermore, the tight constraints on the thickness of the observed plane and its negligible curvature, implies that M/L is a power law function of the observables. The mass-to-light ratio has important implications for galaxy formation (Faber et al. 1987; Djorgovski 1987b) and so one would like to be able to test the assumptions of homology that go into the model.

The observed difference between the FP and the relation predicted from the virial theorem is usually viewed as a systematic variation in the mass-to-light ratio along the FP, given by $M/L \sim L^\alpha$, where $\alpha \sim 0.25 \pm 0.05$ (Faber & Jackson 1976; Faber et al. 1987; Djorgovski 1987b), and it has been shown to vary with bandpass (Djorgovski & Santiago 1993; Pahre, Djorgovski & de Carvalho 1995). Many causes of such an effect have been explored and dismissed to varying extents. Possible stellar population differences along the FP (Djorgovski 1987b; Djorgovski & Santiago 1993; Renzini & Ciotti 1993) seem unlikely due to the required fine-tuning of the IMF or M/L required in order to maintain the thinness of the observed FP. A systematic variation in stellar age along the plane could produce the observed tilt, but would require a large conspiracy in the formation of all galaxies of a given mass in order to be consistent with the observed small thickness of the FP.

To examine stellar population effects, Pahre et al. (1995) tested the significance of the mass-metallicity relation (Guzman, Lucey & Bower 1993) along the FP, by constructing a near-infrared FP. Sampling the older distribution of stars, their K-band photometry is less sensitive than optical wave-bands to differences in galaxy metallicity which appear as line-blanketing effects in the optical (Faber et al. 1987). The near-infrared FP obtained did not differ markedly from the optical FP, with the deviation found being attributed to the reduction in metallicity effects between galaxies. This agrees with earlier work by Dressler et al. (1987b), Recillas-Cruz et al. (1990), and Djorgovski & Santiago (1993), where the metallicity effect was shown to be insufficient to explain the entire observed FP departure from the virial plane. This is also shown to be the case with current population synthe-

sis models, where metallicity effects result in only a small tilt in the plane (Worthey 1994).

This has led to investigations that test the assumptions of kinematic and structural homology and measure the influence of such a breakdown upon the FP (Ciotti, Lanzoni & Renzini 1996; Hjorth & Madsen 1995). Pahre et al. (1995) also concluded that systematic departures from structural and dynamical homology amongst the galaxies may be responsible for the departure between the observed and the virial form of the FP.

Capelato, de Carvalho & Carlberg (1995), using computer model simulations of merged galaxies, claim that the slope of the FP is largely explained by broken homology in the velocity distribution. However, Ciotti et al. (1996) and Ciotti & Lanzoni (1996), using spherical models with the velocity anisotropy described by the Osipkov-Merritt formula, find it is unlikely that orbital anisotropy plays a major role in producing the FP tilt. Anisotropy in the velocity distribution has also been rejected by Djorgovski & Santiago (1993) as the sole cause for the $M/L \sim L^\alpha$ relation. Ciotti et al. (1996) suggested that a systematic trend in the shape of the elliptical galaxy light profiles seems to be the best explanation.

This possibility has been entertained before (Djorgovski, de Carvalho, & Han 1988; Djorgovski & Santiago 1993), but differing profile shapes causing the tilt of the FP has not been explored with observational data. Hjorth & Madsen (1995) parameterised broken structural homology in their models of elliptical galaxies based on the statistical mechanics of violent relaxation (Hjorth & Madsen 1991). They found that for a given correlation between the galaxy structure and its luminosity, such non-homology is not inconsistent with the observed FP having a constant M/L . Unfortunately, their data set did not enable them to draw firm conclusions. There is, however, a growing wave of data supporting the existence of broken structural homology, amongst dwarf galaxies (Davies et al. 1988; Binggeli & Cameron 1991), spiral bulges (Capaccioli 1987; Capaccioli 1989; Andredakis, Peletier & Balcells 1995; Courteau, de Jong & Broeils 1996), elliptical galaxies (Michard 1985; Caon, Capaccioli & D'Onofrio 1993; Burkert 1993; Hjorth & Madsen 1995), and brightest cluster galaxies (Schombert 1986; Graham et al. 1996).

In this paper, using a set of observed surface brightness profiles and measured velocity dispersions, we explore the influence of broken structural and dynamical homology upon the FP. Using the Sersic $R^{1/n}$ light profile (Sersic 1968), the generalised form of the de Vaucouleurs $R^{1/4}$ law (de Vaucouleurs 1948, 1953) with n a free parameter, we can allow for structural differences between galaxies. The $R^{1/4}$ law has two parameters which act as physical scales, scaling the radius and the surface brightness and leaving the profile shape fixed. The $R^{1/n}$ profile has the additional parameter, n , which permits different shapes for the galaxy light profile and therefore allows us to examine broken structural homology amongst galaxies. The Sersic law can take the form of both an exponential disk ($n=1$) and the de Vaucouleurs light profile ($n=4$). It can also approximate a power-law and provides intermediate forms between these common profile shapes by varying its shape parameter n . Caon et al. (1993) and Graham et al. (1996), and references therein, have shown that a range in galaxy profile shapes does exist,

and more importantly that a systematic trend between profile shape and galaxy size exists such that the larger galaxies have less curvature in their light profiles than the smaller galaxies. In this paper we examine the effect of this on the FP. We also explore the use of volumetric galaxy parameters as well as using the standard projected quantities. It is possible to obtain the three dimensional structural quantities by deprojecting the $R^{1/n}$ light profiles (Ciotti 1991). The volumetric kinematical quantity is derived from application of the Jeans hydrodynamical equation to the $R^{1/n}$ model, calibrated by the projected central velocity dispersion.

In section 2 we describe our sample of elliptical galaxies and the derivation of their structural parameters. An overview of the parameters used in the construction of the FP and their relation to the ideal virial plane parameters is given in section 3. We use multivariate statistics to describe and construct the FP in section 4. Our results are discussed in section 5, and our conclusions presented in section 6.

2 DATA

2.1 Surface Brightness Profiles

For the purposes of this investigation we have chosen the small but very high-quality data set of Bower, Lucey & Ellis (1992). The aperture magnitude profiles of 26 E/S0 Virgo cluster galaxies were selected, due to the quality of this CCD data (with an rms internal scatter of 0.015 mag) and as published dynamical data is also available for these galaxies (Dressler 1984, 1987; McElroy 1995).

We took the tabulated V band profiles, and corrected them for the galactic absorption and redshift terms as follows. We applied the K-correction as detailed by Bower et al. (1992), being $\Delta V = 0.005$ mag for Virgo. Galactic extinctions in B-band (A_B), taken from Burstein & Heiles (1984) and Burstein et al. (1987), were applied to our data such that $A_V = 0.75A_B$ (Sandage 1973). For those galaxies not listed, we used the NASA/IPAC Extragalactic DataBase (NED) to find their extinction. We also applied the corrective term for redshift dimming, being -0.013 mag for Virgo at a redshift of 0.003. So as to remove the data most affected by seeing, we truncated the inner profile, excluding data within 3 seeing FWHM. Each galaxy profile consisted of 14 data points before allowances were made for seeing, which resulted in the removal of between 2 to 5 inner data points. The outer data point is given by the largest aperture fitted by Bower et al. (1992), having a diameter of 79 arcsec.

2.2 Galaxy Parameters

We have used the velocity dispersion data in Table 11 of Bower et al. (1992), which comes from Dressler (1984, 1987). We note that an effective aperture of 16×16 arcsec was used to make these measurements (Dressler 1984). Four of the galaxies were not measured by Dressler (marked in Table 2) and so we have used the mean central velocity dispersion given by McElroy (1995), correcting it to the standard used by Dressler. From Table 2 of McElroy (1995), this implies dividing the central velocity dispersion value of McElroy by 1.02 to obtain the value which would have been measured using Dressler's system.

We obtained the effective radius, R_e , and mean surface brightness, Σ_e , within R_e (expressed in linear units rather than mag arcsec $^{-2}$) by fitting an $R^{1/n}$ model profile (Sersic 1968) to the corrected luminosity profiles. The form of this profile is

$$I(R) = I_e \exp \left\{ -b \left[\left(\frac{R}{R_e} \right)^{1/n} - 1 \right] \right\}, \quad (1)$$

where I_e is the intensity at the radius R_e . The parameter b is chosen so that R_e is the projected radius enclosing half the total light from the galaxy and is well approximated by $b = 1.9992n - 0.3271$ (Capaccioli 1989).

The aperture magnitude, within radius R , is obtained from the projected luminosity within a circular aperture of this radius. The luminosity within a radius R , is then calculated from $2\pi \int_0^R I(R) R dR$. Using the change of variable $x = b(R/R_e)^{1/n}$, it can be shown that

$$L(R) = 2\pi n \frac{e^b}{b^{2n}} \gamma(2n, x) I_e R_e^2, \quad (2)$$

where γ is the incomplete gamma function. The galaxy light profiles of Bower et al. (1992) are in the form of aperture magnitudes, and we used a standard non-linear least squares fit (i.e. minimisation of the ordinate to define the best fitting line) to obtain the model parameters R_e , $\mu_e (= -2.5 \log I_e)$, and n , from the equation

$$m(r) = C - 2.5 \log \gamma(2n, x), \quad (3)$$

where $C = -2.5 \log [I_e R_e^2 2\pi n e^b / b^{2n}]$. The residuals of the aperture magnitude data points about the best-fitting $R^{1/n}$ profiles are shown in Figure 1. There were multiple observations of individual galaxies, and we show the residual profiles for each set of data for each galaxy.

The model parameter R_e (arcsec) was converted to kpc using a Virgo redshift of 0.003, and $H_0 = 75 \text{ km s}^{-1} \text{ Mpc}^{-1}$. As R_e is sometimes larger than our observed outer radius data point of 39.5 arcsec, one cannot always simply integrate the profile data out to R_e in order to get Σ_e . An alternative approach was developed based upon the surface brightness profile from the $R^{1/n}$ model (see Appendix A). Such extrapolation is valid given the assumption that the $R^{1/n}$ model is suitable beyond our observed outer radial point and out to the model half-light radius R_e . For Virgo, 39.5 arcsec corresponds to 2.28 kpc, and roughly 1/3 of our sample required an extrapolation. We averaged the model parameters when multiple observations existed, obtaining a single mean value to represent each galaxy. Agreement between different observations of similar galaxies is good. This can be seen in Table 1, or more easily in Figure 3, where the $1\sigma \chi^2$ confidence intervals of the fitted model parameters overlap each other for multiple images of the same galaxy.

We have plotted the logarithm of the average shape parameter n , obtained from the models fitted to the galaxy profiles, against the logarithm of the average spatial half-light radius in Figure 2. As seen in the following section, the spatial half-light radius is approximately $1.34R_e$ for all values of n . That is not to say the spatial half-light radius is independent of n , as it is n that determines the profile shape and thus the value of R_e and the spatial half-light radius. Also shown in the $n - \log R_e$ plane are the 1σ confidence regions for the fitted model parameters of every image. These are based upon the projected $\Delta\chi^2 = 2.30$ contour around

the best fitting solution (n, R_e, μ_e), after normalising the reduced χ^2 to 1 at the fitted minimum (Figure 3). Saglia et al. (1996) point out that under certain conditions, such χ^2 contours can underestimate the true errors. This effect becomes increasingly apparent as the actual galaxy light profile departs further and further from the assumed model profile (an $R^{1/4}$ law in their analysis of this effect). In fitting an $R^{1/n}$ model, we explicitly allow for such an effect (to the extent that the $R^{1/n}$ model can correctly fit the data) and hence reduce the influence of this effect on our estimated errors. Saglia et al. (1996) note that the discrepancy is mainly due to large extrapolations of the fitted profile models in obtaining quantities like total galaxy magnitude. We do not compute the total galaxy magnitude, and consequently our model parameters are largely free from such extrapolations. Although $R_{e,n}$ is the half-light radius it does **not** require the total magnitude for its derivation, which comes directly from the luminosity profile fit. A few galaxies did require some extrapolation, but only as far as their model half-light radii. We note that these model half-light radii may not be the true galaxy half-light radii, as we don't have detailed extended photometry and the $R^{1/n}$ model may not be appropriate for the faint outer parts of the galaxy, where galaxy envelopes or halos may result in a departure from the inner profile shape. The model radii obtained *are* however representative of the brighter inner portions of the galaxy profile and are useful for our analysis. Whilst there is a coupling between the galaxy model parameters (although we note that a couple of the larger contours in Figure 3 have the effect of dominating this picture), such coupling cannot fully explain the observed trend. The value of n clearly increases with effective radius.

Bower et al. (1992) made multiple observations of the 26 galaxies in the data sample. Table 1 lists the model parameters for every observation. The average values used in the construction of the FP are listed in Table 2, along with the observed central velocity dispersions. The values in Table 2 have been transformed from projected quantities into spatial quantities, as detailed in the following section.

2.3 Possible sky-subtraction errors

We explore the possibility that sky-subtraction errors may be leading to the observed departures from an $R^{1/4}$ profile. Even with all of the care that the Bower et al. (1992) data was put together, the use of small area detectors can leave residual sky-subtraction errors. Perhaps the larger galaxies, with apparently greater values of n , are a product of systematically larger sky-subtraction errors which mimic departures from an $R^{1/4}$ law.

To investigate this, we fitted the galaxy profile data with the model

$$I(R) = I_e \exp \left\{ -7.669 \left[\left(\frac{R}{R_e} \right)^{1/4} - 1 \right] \right\} + I_{sky}, \quad (4)$$

which is the standard $R^{1/4}$ law plus an intensity term for the possible sky-subtraction residual (which can be either positive or negative in this equation). Sky-subtraction is a common concern, and an incorrect value for the sky brightness will result in changes to the derived galaxy magnitude profile. The addition of an extra parameter in the profile fitting, namely I_{sky} , will of course produce more accurate fits

as governed by the χ^2 statistic. The question is whether or not this extra parameter (actually a correction) is justifiable.

Plotted in Figure 4 is the ratio of the χ^2 fit from the $R^{1/4}$ + sky-correction model to the χ^2 fit from the simple $R^{1/4}$ model. Also shown is the ratio of the χ^2 fit from the $R^{1/n}$ model to that from the simple $R^{1/4}$ model. Both of the additional models, containing a third parameter, clearly show an improvement in fit when one deviates from an $n=4$ profile. The question to be addressed here is whether use of the sky-corrected $R^{1/4}$ model can be substantiated. We turn our attention to the size of the sky-subtraction correction that these models imply.

The photometry comparison with previous authors work, which Bower et al. (1992) performed, puts a limit on the size of possible errors. Even if we attribute the entire disagreement between observers work to sky-subtraction errors, we still have quite stringent limits. Aaronson, Persson & Frogel (1981), using large photographic plates rather than small area CCD's, obtained V-band data for 22 Virgo galaxies in common with the sample of Bower et al. (1992). Rejecting 2 out lying points, Bower et al. (1992) found a scatter of only 0.035 mag in the comparison photometry. A similar scatter of 0.036 mag was found with the comparison of Michard (1982) (also with 20 common galaxies). Even if we attribute all of this scatter to sky-subtraction errors by Bower et al. (1992), we still have a very tight constraint on the allowed sky-subtraction errors in our profile models. Figure 5 shows that the majority of sky-subtraction errors are notably larger than permitted by our quite liberal error allowance. So while the addition of a sky-subtraction correction produces improved fits to the data, it is not justified.

The introduction of this additional parameter has the success it does because it is mimicking, to some degree, the effect of some other real physical process or situation. Whilst an $R^{1/4}$ law is being fitted in these models, it is being done coincidentally with a term that effectively re-shapes the profile to obtain an $R^{1/4}$ profile. In this fashion, the model incorporating a sky-correction term is able to allow for real differences in galaxy profile shapes, as better represented by the $R^{1/n}$ law (Caon et al. 1993; Graham et al. 1996) In Figure 6, we show that the $R^{1/4}$ + sky-correction model is only superior to the $R^{1/n}$ model for unacceptably large under-estimations of the sky background level. Also, 13 of the points in Figure 6 for which the $R^{1/4}$ + sky-correction model is superior to the $R^{1/n}$ model belong to just one galaxy (NGC 4552), which was observed 14 times; 6 of these points occupy the cluster of 8 points that favour the $R^{1/4}$ + sky-correction model. Removal of NGC 4552 eliminates the impression that use of an $R^{1/4}$ + sky-correction model is generally better than the $R^{1/n}$ model when one is dealing with the larger galaxies ($n > 4$).

In further support of our conclusion that sky-subtraction errors are not the effect responsible for the range in profile shapes seen, Capelato et al. (1995) also found a correlation between n and R_e . The $R^{1/n}$ models they fitted to their computer simulated elliptical galaxy merger remnants, have no uncertainty as to sky levels, thus eliminating this possibility. There is however another possibility as to the cause of the range in our profile shapes. S0 galaxies are known to possess a disk as-well as their central bulge. If our sample of galaxies contained significant disks and a range of bulge-to-disk ratios, then this might explain the apparent

broken structural homology (Saglia et al. 1996). Whilst this could be so, an argument against such an origin is that the galaxy models of Capelato et al. (1995) were disk free, as was the work with Brightest Cluster Galaxies by Graham et al. (1996), where a large range in profile shapes was still evident. Also, given the observed trend with n and R_e , one would have to claim that the disk-to-bulge ratio increased for the bigger galaxies, which it does not (Andredakis, Peletier & Balcells 1995).

3 THEORY

3.1 Overview

A good summary of the relation between the observed and the virial planes can be found in Djorgovski, de Carvalho & Han (1988), and we adopt their method of analysis in what follows. From the virial theorem, the connection between the potential and kinetic energy can be written as

$$\frac{GM}{\langle R \rangle} = k_e \frac{\langle V^2 \rangle}{2}, \quad (5)$$

with M and $\langle R \rangle$ being a measure of the galaxy mass and radius, respectively, such that $GM/\langle R \rangle$ is the galaxy potential energy and $\langle V^2 \rangle/2$ is the mean kinetic energy per unit mass for the galaxy. k_e is a virialisation constant reflecting the degree to which the system is virialised. Galaxy mergers and the process of violent relaxation redistribute the orbital energy of the stars. Galaxies may exist in a quasi-static equilibrium, with varying degrees of energy dissipation or in varying stages of relaxation, and hence varying values of k_e may exist before a galaxy settles down into virial equilibrium ($k_e=2$) (Djorgovski et al. 1988). In addition to this, the k_e term also allows for possible neglect of rotational energy: in our use of central velocity dispersions to measure the kinetic term, $\langle V^2 \rangle$, we have ignored possible contributions from the rotational energy of each galaxy.

A choice now arises regarding which observables one uses to fit for the quantities M , $\langle R \rangle$ and $\langle V^2 \rangle$.

3.2 Structure

For elliptical galaxies, an observed radius R (such as R_e) is typically used to approximate $\langle R \rangle$ such that

$$R = k_R \langle R \rangle. \quad (6)$$

The parameter k_R allows for the possibility that our observed projected radius R may not be equal to the physical radius we wish to use. k_R depends on the mass-density structure of the galaxy, allowing for variations in the distribution of matter from one galaxy to the next. It is possible that different galaxies formed with a different mass-density structure. It is also likely that evolutionary processes such as galaxy merging and tidal interactions have further modified the k_R term. By addressing the breakdown of structural homology between galaxies, we can explore the variations in the k_R term. These variations, if ignored, introduce systematic errors into the parameterisation of elliptical galaxies, and hence into the construction of the FP.

The central velocity dispersion, σ_0 , is used to represent the kinetic energy term such that

$$\sigma_0^2 = k_V \langle V^2 \rangle, \quad (7)$$

with k_V reflecting the dynamical structure within the galaxy. Like the k_R term, the k_V term reflects the formative and various evolutionary processes that have shaped the galaxy. It incorporates the anisotropies of the velocity dispersion tensor, including the differing degrees of random and circular motion in the galaxy, and differing velocity dispersion profiles.

Lastly, we have

$$(M/L)\Sigma R^2 = \frac{1}{k_L}M, \quad (8)$$

where (M/L) is the global galaxy mass-to-light ratio, and k_L incorporates the luminosity structure within the galaxy. Σ is an intensity term, obtained from the fitted light profile.

Substitution into equation 5 gives

$$R = K_{SR}\sigma_0^2\Sigma^{-1}(M/L)^{-1}, \quad (9)$$

with

$$K_{SR} = \frac{k_e}{2Gk_Rk_Lk_V} \quad (10)$$

being the combined structural term appropriate for this expression, as given by Djorgovski et al. (1988). Without knowledge of the K_{SR} term, it has, in the past, been assumed a constant, and the observed departures of the FP from the relation $R \propto \sigma_0^2\Sigma^{-1}$ have been attributed to (M/L) , perhaps with an additional comment as to uncertainties about assumed structural and dynamical homology. This paper advances the work of Djorgovski et al. (1988), where they proceeded under the assumption of homology (i.e. that all the k 's are constant) - we do not. Through fitting an $R^{1/n}$ profile which specifically allows for structural differences, there is no assumption of structural homology. We point out that whilst the $R^{1/n}$ profile covers an extensive range of profile shapes, it does not cover every possible profile shape as that would require an endless number of parameters in the fitted profile model. Thus, we only explore broken structural homology as far as the $R^{1/n}$ model allows, which turns out to be quite sufficient. Allowing for variability in the profile shapes, we can now better address the k_R and k_L terms, and also have a better representation for the k_V term.

We explore the use of spatial (i.e. three-dimensional) quantities to represent $\langle R \rangle$, M , and $\langle V^2 \rangle$. We take the spatial half-mass radius, $r_{1/2}$, which is equivalent to the spatial half-light radius for a constant M/L , to represent $\langle R \rangle$. We compute the total galaxy luminosity, and use the assumption of constant M/L to obtain half the total galaxy mass which is used to represent M . The spatial velocity dispersion at $r_{1/2}$ is acquired using the Jeans equation (see Section 3.2) and is used as our estimate of $\langle V^2 \rangle$. These quantities are not directly observable, but they can be computed from other observable quantities given a knowledge of the k -terms.

Ciotti (1991) related the luminosity form of the Sersic law to its underlying mass-density structural form, by solving the Abel integral equation (Binney & Tremaine 1987) which relates the projected/deprojected expressions. He also computed the spatial half-mass radius $r_{1/2}$ for differing exponents n , and found that this radius, divided by the projected effective radius R_e , is practically a constant value (ranging from 1.339 to 1.355 for $n=2$ to 10). We note a sim-

ilar figure was also found for the Jaffe (1983) models (1.311) and the Hernquist (1990) models (1.33). Thus, the spatial half-light radius (in units of R_e) is largely independent of the variant forms of the mass-density distributions used to describe the galaxy and so k_R can be taken to be a constant with

$$R = R_{e,n} \approx (1/1.34) < R > = 0.75r_{1/2}. \quad (11)$$

This is not to say that $r_{1/2}$ is independent of n and therefore does not depend on the galaxy profile shape. What it does say is that $r_{1/2}$ is dependent on the projected half-light radius, which is very much dependent on the profile shape and hence the value of n .

The structural term k_L is not as simple, but it can be computed for different values of n . Using $M = M_{tot}/2$ and $(M/L) = (M_{tot}/L_{tot})$ in equation 8, upon substitution of L_{tot} from equation 2 (where the incomplete gamma function, γ , becomes the gamma function Γ), we have

$$k_L = \pi n \Gamma(2n) e^b / b^{2n}. \quad (12)$$

As b is well approximated by a simple linear function of n ($1 < n < 10$), we have an expression for the luminosity structural term in terms of the shape parameter n . Allowances for different galaxy luminosity structures are made to the mean intensity term Σ , which is fed into the FP as the surface brightness parameter. This is achieved by using $\mu_e - 2.5 \log(k_L)$, rather than μ_e (the surface brightness at R_e) which does not fully represent the luminosity structure (as detailed in equation 8). If all galaxies did obey an $R^{1/4}$ law, then the difference between these terms would just be a constant and use of one term over another would not effect the tilt of the FP.

The mean surface brightness, $\langle \mu \rangle_e$, within the effective radius, R_e , is related to the intensity by $-2.5 \log \langle I \rangle_e$, where $\langle I \rangle_e = L_{tot}/2\pi R_e^2$ from Appendix A. In Appendix A, we also see that $\langle \mu \rangle_e - [\mu_e - 2.5 \log(k_L)] = 2.5 \log(\pi)$, independent of the value of n . Thus $\langle \mu \rangle_e$ can be used in the construction of the FP, instead of $\mu_e - 2.5 \log(k_L)$. The intercept of the FP will be effected but not the slope of the plane.

Thus, to the extent that the $R^{1/n}$ model represents the observed variations in structural form, we are able to address two of the components that go into making the K_{SR} term which determines differences between the observed and the virial plane. The $R^{1/n}$ model parameters, R_e and $\langle \mu \rangle_e$ implicitly allow for these variations in profile shape which is explicitly represented by the third model parameter n .

3.3 Dynamics

As we do not confront the issue of orbital anisotropy, we cannot fully address the k_V term, although we do partially deal with it by tackling the problem of differing velocity dispersion profile shapes due to differing luminosity profiles, as represented by the $R^{1/n}$ model. Dynamical homology implies that each galaxy has the same fall off in velocity dispersion away from its center. It is therefore obvious that broken structural homology necessitates broken dynamical homology. Working with the assumptions of spherical symmetry and isotropic pressure support, Ciotti (1991) has shown how both the spatial velocity dispersion profile and the projected line of sight velocity dispersion profile change with radius

for a series of $R^{1/n}$ models with a range of shape parameters from 2 to 10. We do not deal with possible dynamical anisotropies within each galaxy, as this requires detailed spectral mapping and/or assumptions about the ratio of the radial to azimuthal velocity dispersion (Ciotti, Lanzoni & Renzini 1996).

There is of course the additional concern of an aperture effect. Even if all galaxies did have the same velocity dispersion profiles, as one samples galaxies that are further away, the fixed aperture size on the sky will sample a larger portion of the galaxy. This has been addressed by Dressler (1984) and Davies et al. (1987), and is implicitly taken into account in what follows. However, the problem is more complicated than this. What one would actually like to do, is not be consistent in using the same physical aperture size on each galaxy, but to sample each galaxy with the same ratio of aperture size to half-light radius[†] (Wegner et al. 1996). That is, to always measure the velocity dispersion within say, $1R_e$ or $0.2R_e$ or some fixed ratio of R_e . It is clear that use of core velocity dispersion measurements is inadequate in representing a galaxies overall kinematic state.

Extending the work of Ciotti (1991) we compute the projected aperture velocity dispersion as a function of the ratio of the aperture size to the projected half-light radius, as shown in Figure 7 (The details are left for Appendix B). From these models, the ratio of the projected aperture velocity dispersion (of aperture size equal to that used to obtain the central velocity dispersion at the telescope) to the spatial velocity dispersion at $r_{1/2}$, can be used to correct the measured central velocity dispersion to the spatial half-mass value. This ratio is shown in Figure 8. Depending on the aperture size used (actually the ratio of the aperture size to the projected half-light radius), use of the measured central velocity dispersion by itself may result in departures of a factor of 2 or 3 from the spatial half-mass velocity dispersion measure.

It is possible to estimate the galaxy masses, using our measures of galaxy size and velocity dispersion. Once we have fitted the galaxy luminosity profile with an $R^{1/n}$ law, the only unknown in equation B8 is (M/L) , where we have used our measured central velocity dispersion for $\sigma_{ap,n}^2(R_{ap})$ and the value predicted by theory, shown in Figure 7, for $\sigma_{ap,n}^2(\eta_{ap})$. Substituting in the total galaxy luminosity for L , from equation 2, we can then solve for the total galaxy mass M_{tot} . Figure 9 shows the total galaxy mass obtained in this way, plotted against the shape parameter n .

We also use the model velocity dispersion profiles and the observed central velocity dispersion to compute the aperture velocity dispersion extended to infinity, $\sigma_{tot,n}$. Ciotti (1994) shows this quantity to be equal to one third of the virial velocity dispersion (in the case of spherical systems) and independent of any possible orbital anisotropy.

Finally, we remind the reader that this paper does not treat the fourth parameter k_e , in equation 10, which allows for different degrees of virialisation and the neglect of rotation.

[†] This correct approach would imply a different conversion of the central velocity dispersion in McElroy (1995) to the standard of Dressler (1984).

4 FUNDAMENTAL PLANE CONSTRUCTION

We construct four planes. The first one is the standard plane, obtained by fitting $R^{1/4}$ profiles, and uses the projected effective radius R_e , the mean surface brightness within this radius, Σ_e , and the measured central aperture velocity dispersion σ_0 . This plane is used as our reference plane, to see how the planes produced by alternate choices of variables change. The second plane that we construct allows for differences in galaxy structure. We fit an $R^{1/n}$ profile, and use the spatial half-light radius, the associated mean surface brightness within this radius, and the central aperture velocity dispersion. Such a plane will tell us the extent to which use of an $R^{1/4}$ law for all galaxies is responsible for the tilt of the FP. The third plane treats broken structural homology and also allows for the fact that a fixed aperture measure for the velocity dispersion will sample different ratios of the area enclosed by R_e , as R_e itself varies between galaxies. Here we transform the central aperture velocity dispersion measure into the spatial half-light velocity dispersion $\sigma_{1/2,n}$. The fourth plane we construct uses the spatial structural parameters from the $R^{1/n}$ model and an infinite aperture velocity dispersion term.

A Principal Component Analysis (PCA) was performed on each 3 dimensional data set, $(\log \sigma_0, \log R_{e,4}, \Sigma_{e,4})$, $(\log \sigma_0, \log R_{e,n}, \Sigma_{e,n})$, $(\log \sigma_{1/2,n}, \log R_{e,n}, \Sigma_{e,n})$, and $(\log \sigma_{\text{tot},n}, \log R_{e,n}, \Sigma_{e,n})$. The code from Murtagh & Heck (1987) was used to show the degree to which the data are defined by a plane in our 3-space of observables. Table 3 shows that greater than 98 per cent of the variance in the data lies in a plane, confirming the appropriateness of constructing a plane to describe the properties of elliptical galaxies.

The method of construction of the plane is not an obvious task and many different approaches have been tried in the past (Djorgovski & Davis 1987; Lynden-Bell et al. 1988b; Lucey, Bower & Ellis 1991a). In the fitting of a plane to 3-space data, one has considerable choice in exactly what it is that one minimizes in order to obtain the ‘best’ plane. One gets a good idea of the problem from Isobe et al. (1990) and Feigelson & Babu (1992), where 6 possible approaches to the fitting of a straight line in a 2-space data set is detailed. The situation is of course worse for higher dimensions. However, extending the ideas learned in 2-space to 3-space, we have a better idea of how to approach the problem.

Our current work wishes to establish the FP for the sake of comparison with what theory, i.e. the virial theorem, predicts. Given this, we do not distinguish any dependent/independent variables, and so we cannot build our plane by minimising the residuals in one variable alone. An approach that considers the residuals in all variables shall be needed, and from the 2 dimensional case studies of Isobe et al. (1990) and Feigelson & Babu (1992), we see that the bisector method of regression is most suited for our needs. For studies requiring symmetrical treatment of the variables, the bisector method of linear regression was found to be the preferred method, having a greater certainty on the slope of the fitted line than other methods, such as orthogonal regression. In this technique, we construct the plane 3 times, each time minimising the residuals of a different observable against the other two observables. The mean slope angles, obtained from the average of the three planes, is then used to represent our ‘best’ FP.

With the FP relation described as

$$\log R_e(kpc) = A \log \sigma - 0.4B \Sigma_e + C, \quad (13)$$

the virial theorem predicts that A should be 2 and B should be -1. The observed FP, as determined by the bisector method, for our four data sets described above, is shown in Table 4, with the associated uncertainty being the standard error.

Because there is no natural ‘best’ method of construction for the FP, we used an additional method, pioneered by Djorgovski & Davis (1987), as a check. First, the ‘mixing’ value b that gives the highest linear correlation coefficient between $\log R_e$ and $(\log \sigma + b \Sigma_e)$ is obtained. We used the bootstrap method to estimate the standard error on b . It is then possible to treat the problem as a 2-dimensional least-squares problem. The program SLOPES, from Feigelson & Babu (1992), was used to compute the best fitting line for a multitude of methods: ordinary least squares of y on x OLS($y|x$), and the inverse OLS($x|y$), the line which bisects these two, minimisation of the perpendicular residuals (known as orthogonal regression) the geometric mean of OLS($y|x$) and OLS($x|y$) (referred to as the reduced major axis regression line) and finally the arithmetic mean of the OLS lines. The reader is referred to their paper for a discussion of each method, for which the slopes and errors are computed using three techniques. The first technique uses the linear regression formulae, but as these can underestimate the slope variance for small data samples, a bootstrapping simulation and a jackknife analysis are also performed. The various solutions are displayed in Table 5. The value of A in equation 13 is explicitly shown and the value B is calculated such that $B = -2.5 \times b \times A$, where b is the ‘mixing’ value mentioned above.

To represent the method of analysis using the mixing parameter, we use the orthogonal regression solution from Table 5, consistent with the method of Pahre et al. (1995), as the one method from the possible 6. The bisector method should perhaps be used, given the discussion in Feigelson & Babu (1992), but the differences between these two planes are within the errors. This orthogonal method gives similar planes to those found with our 3D method of analysis. Figure 10 shows the various FPs constructed using our 3D bisector method. Figure 10a uses the standard data set from the $R^{1/4}$ fits and the central aperture velocity dispersion measures, whilst Figure 10b uses the data set from the $R^{1/n}$ fits and the central aperture velocity dispersion. Figures 10c, 10d use the spatial parameters from the $R^{1/n}$ fitted model along with the spatial half-light velocity dispersion term and the infinite aperture velocity dispersion term respectively.

5 DISCUSSION

The additional parameter, n , in the $R^{1/n}$ light profile models, is shown to have a physical association with the galaxies’ other properties, such as size and mass, as seen in Figure 2 and Figure 9. The bigger galaxies have larger values of n , and thus less curvature in their light profiles, as previously shown by Caon et al. (1993) and Graham et al. (1996). Not allowing for variations in profile shape can have a substantial systematic effect on the derived half-light radius and asso-

ciated surface brightness term. Figure 11 shows the ratio of the half-light radius derived using the $R^{1/n}$ model to that obtained using the $R^{1/4}$ model, plotted against the model value of n . One clearly sees that assuming an $R^{1/4}$ law for the larger galaxies will result in an underestimate of the effective radii. So too, use of the $R^{1/4}$ law on the smaller galaxies will lead to over-estimates for the galaxies' effective radii. If the galaxy luminosity profile is best described by a value of n greater than 4, the effective surface brightness will be too bright if an $R^{1/4}$ profile is applied. Likewise, the effective surface brightness term from an $R^{1/n}$ profile is fainter than that from the $R^{1/4}$ profile when n is less than 4. Allowing for structural differences has the result of producing a greater range in both radius and surface brightness.

With the introduction of this additional parameter, we performed another Principal Component Analysis to determine the optimal number of dimensions in the 4-space ($n, \log R_{e,n}, \Sigma_{e,n}, \log \sigma_0$). The major eigenvector contained 67 per cent of the variance, and the second dominant eigenvector had 27 per cent. Thus, our 4-space of observables is still well represented by a two dimensional plane, encompassing 94 per cent of the total variance (use of $\log \sigma_{1/2,n}$ and $\log \sigma_{\text{tot},n}$ gave similar results). Therefore, a hyperplane does not seem warranted. This is not surprising due to the strong correlation seen between n and $\log R_e$ in Figure 2.

If one was to use the FP as a distance indicator, then its method of construction would be different to the method used here. In such a case, one would wish to predict the value of one distance-dependent variable from the measurement of other distance-independent variable(s), and so one should use OLS($y|x$), where y is the variable to be predicted. With this OLS($y|x$) fit we obtained an rms scatter about the plane of 0.09 in $\log R_e$ when an $R^{1/4}$ law was applied with σ_0 , and an rms scatter of 0.10 when an $R^{1/n}$ law and spatial structural quantities were used with $\sigma_{\text{tot},n}$. The uncertainty on these rms scatters is around 0.02, so there is no significant difference in the scatter about the FP using the two methods. We also measured the intrinsic thickness of the FP by computing the rms orthogonal offset of the data points about the plane; here we assume no dependent/independent variables. These rms values are shown in Table 4.

The virial theorem predicts the relation $R \propto \sigma^2 \Sigma^{-1}$, when the surface brightness, Σ , is expressed in linear units rather than mag arcsec^{-2} . Observed planes for cluster galaxy data, using $R = R_e, \Sigma = \Sigma_e$, and $\sigma = \sigma_0$ (the projected central velocity dispersion) have been in good agreement with each other in the past. Dressler et al. (1987b) found $R \propto \sigma^{1.33} \Sigma^{-0.83}$ for 6 combined galaxy clusters, with Lucey et al. (1991a) obtaining $R \propto \sigma^{1.27} \Sigma^{-0.78}$ for a Virgo subsample ($\mu_e(B) < 22.00$) of 16 ellipticals. Lucey et al. (1991b) found a similar result for their V -band study of 51 ellipticals in Coma, with $R \propto \sigma^{1.23} \Sigma^{-0.82}$ and a larger study of 11 clusters by Jørgensen, Franx & Kjaergaard (1996), taken in Gunn r , produced an identical result.

A recent near-infrared study of 5 nearby clusters (59 elliptical galaxies) by Pahre et al. (1995) gave $R \propto \sigma^{1.44} \Sigma^{-0.79}$. This steeper slope of the plane was attributed to a reduction of metallicity effects in the near-infrared band-pass compared to the optical. Intriguingly, they obtained the notably different $R \propto \sigma^{1.62} \Sigma^{-0.93}$ for their Virgo sample of galaxies. As this sample only numbered 8 galaxies,

this result does not carry much weight on its own, but does warrant further investigation.

As shown in Table 4, allowing for structural homology through use of an $R^{1/n}$ profile, and maintaining use of the central velocity dispersion, *actually increases* the departure of the FP from the virial plane. Whilst the radial term changes in the sense that it reduces the departure, the surface brightness term works to increase the departure and proves to be the dominant effect. However, changes to the structure of a galaxy imply changes to the velocity field of the galaxy. These changes can be obtained through application of the Jeans equation for a pressure-supported system.

One problem with the use of central velocity dispersions is that they sample different portions of the half-light radius for each galaxy. To be consistent in our measuring of galaxy parameters, we computed all parameters at the spatial half-light radius. This meant converting central aperture velocity dispersions into the associated value at the spatial half-light radius (see Appendix B for details). Doing this, and using the spatial parameters from the $R^{1/n}$ profiles, we found that the FP constructed from these quantities more closely resembled the virial plane. The exponent on the surface brightness term in this expression for the FP is consistent with the virial theorem prediction of -1. Past differences between this exponent and the virial expectation can be explained by systematic departures from structural and dynamical homology and the use of projected rather than volumetric velocity dispersion. The exponent on the σ term is closer to the value expected from the virial theorem, changing from 1.33 to 1.48 as we allow for such changes, but it does not reach the expected value 2.

Although use of the spatial half-light velocity dispersion for all galaxies is consistent and methodical, and preferred to the use of central velocity dispersion measures, it is still arbitrary. We have therefore derived the total aperture velocity dispersion (i.e. the value of the aperture velocity dispersion at infinite radius), which for spherical systems is equal to one-third of the (three dimensional) virial velocity dispersion (Ciotti 1994). The FP that allows for differences in galaxy profile shape and uses the total aperture velocity dispersion more closely resembles the virial plane, $R \propto \sigma^2 \Sigma^{-1}$, than the standard observed plane obtained with $R^{1/4}$ law parameters and central aperture velocity dispersions. The respective planes are described by $R \propto \sigma^{1.44 \pm 0.11} \Sigma^{-0.93 \pm 0.08}$ and $R \propto \sigma^{1.33 \pm 0.10} \Sigma^{-0.79 \pm 0.11}$.

Capelato et al. (1995) found, using computer simulations to build and merge elliptical galaxies, that as they increased the aperture size in which they measured the velocity dispersion term, the difference between the FP they built and that predicted by the virial theorem was reduced. Although the initial conditions of their models were somewhat limited and their range of merged galaxies does not fully represent the range of elliptical galaxies we see today, their work strongly indicates that the assumption of homology amongst elliptical galaxies is invalid. They effectively held constant the stellar population, did not alter the IMF or M/L ratios, and have no metallicity effects to worry about in their dissipationless models. The tilt of the FP in their models is therefore not due to any of these effects. Their work implied that most of the nonhomology lies close to the center of their merged galaxy models, and hence use of larger apertures gives a more accurate picture of the viri-

alised system — thus the reduction between the observed and virialised planes found with the use of a larger aperture. A similar physical effect could be occurring with our use of an effectively larger aperture, albeit an infinite aperture dispersion based on transforming the central aperture dispersion using the $R^{1/n}$ light models, compared to the average aperture size of only $0.2R_e$ that has been used in the past.

Although our model velocity dispersion profiles allow for different distributions, as described by the $R^{1/n}$ model, they are built upon certain assumptions, and we have not dealt with possible orbital anisotropies, as would have been done implicitly in the computational work of Capelato et al. (1995). In examining the structural and dynamical deviations from homology between the progenitor and merged galaxy models, Capelato et al. (1995) claim the nonhomologous velocity dispersion profiles as the main cause of the tilt to the FP. However, their merger remnants only spanned a range in n from 1.2 to 3.4, so they have not really explored the full range of structures observed in nature, and cannot entirely exclude this as a contributing factor to the tilt of the FP.

Ciotti et al. (1996) and Ciotti & Lanzoni (1996) concluded that velocity anisotropy cannot cause the observed FP tilt by itself (i.e. if structural homology is assumed). This result was derived from a range of theoretical galaxy models (including the $R^{1/n}$ model) and introducing varying amounts of orbital anisotropy as described by the Osipkov-Merritt parameterisation (Osipkov 1979; Merritt 1985). Ciotti & Lanzoni (1996) did however suggest an observational test for possible velocity anisotropy effects, namely the use of large apertures to measure the velocity dispersion term, an idea supported by Capelato et al. (1995) and incorporated in this study. Our work suggests that the combination of broken homology in both the surface brightness and dispersion profiles of elliptical systems is partly responsible for the departure of the observed FP from the predicted plane.

These results have implications for most studies that have been done to date using the FP, or the $D - \sigma$ relation, because such studies have assumed structural homology and used projected quantities. Studies of the peculiar motions of elliptical galaxies in the local Universe (Lynden-Bell et al. 1988b; Lucey & Carter 1988; Dressler & Faber 1990) now warrant re-examination, as such measurements may be systematically affected by biases in the distance indicator relations. Furthermore, studies of environmental dependence on the $D - \sigma$ relation and differences between field and cluster ellipticals (Silk 1989; Djorgovski et al. 1988; Lucey et al. 1991b; Burstein, Faber & Dressler 1990; de Carvalho & Djorgovski 1992) can be re-examined. If the galaxy structure is dependent on the galaxy environment, then the $D - \sigma$ relation may also be dependent on environment. However, in fitting an $R^{1/n}$ profile, we have already taken into account different galaxy structures (and so possibly different galaxy environments). Thus the new FP which we derive may implicitly take into consideration some environmental effects, although not stellar population differences (Guzman & Lucey 1993; Guzman et al. 1993) or intrinsically different M/L ratios in different clusters (Kaiser 1988). It will of course be of interest to obtain data from other clusters, and field galaxies, to investigate such possibilities.

Working with the simplification that the K_{SR} term in equation 9 is now a constant (although it still contains the k_e and k_V terms which we have not properly dealt with) we can compute the mass-to-light ratio, assuming it is a power law function of the observables. For the plane constructed from the $R^{1/4}$ law model and using the central aperture velocity dispersion measure, we have that $M/L \sim L^{0.25}\Sigma^{-0.06}$; whereas for the plane that was constructed allowing for broken structural homology and using the volumetric quantities, we find that $M/L \sim L^{0.17}\Sigma^{0.17}$, or that $M/L \sim \sigma^{1/2}$. For the plane that used $R^{1/n}$ model parameters and the total aperture velocity dispersion measure we have that $M/L \sim L^{0.20}\Sigma^{0.09}$. Of course it may be that M/L is constant and it is the K_{SR} term in equation 9 that varies with L and Σ or σ , as mentioned previously, or it may be that terms are varying.

The tilt of the FP is probably due to a combination of factors. For instance, whilst Pahre et al. (1995) did not recover the virial plane in their construction of the near-infrared FP, they did measure a change in α , with $M/L \sim M^\alpha$, from 0.23 (Lucey et al. 1991b; de Carvalho & Djorgovski 1992) in the optical (V-band) to $\alpha=0.16$ (K-band). They found that the exponent on the velocity dispersion term, A , increased by 0.19 ± 0.06 dex from the V-band to the K-band (cf. $+0.29 \pm 0.11$, Djorgovski & Santiago (1993)).

Whilst we have dealt with the effects of seeing on the galaxy light profile, by excluding data within the central radius of 3 FWHM, we have not dealt with the seeing effect on the central velocity dispersion measurements. As an effective 16×16 arcsec aperture was used to obtain the velocity dispersion for our sample (Dressler 1984, 1987), seeing should not be a problem. However, studies using a single smaller aperture (say 2×4 arcsec) may be effected by seeing if there is a steep velocity dispersion gradient present (Whitmore 1980; Jarvis & Peletier 1991).

Several other issues must be kept in mind: the galaxies may not be virialised; we have not dealt with the matter of rotational support (as opposed to pressure support); the issue of broken dynamical homology has not been fully treated, as we assumed orbital isotropy; stellar population variations with galactic radius may result in (M/L) varying with radius; or light may not trace mass in a simple fashion. Any combination of these effects may work in symphony to account for the FP tilt.

6 CONCLUSIONS

A range in profile shapes is found to exist for the sample of 26 elliptical galaxies used in this study. The shape parameter n is found to have a physical association with galaxy size and mass, in the sense that a larger value of n corresponds to a larger galaxy. Allowances for different profile shapes and the use of infinite aperture velocity dispersion measurements, which allow for different velocity dispersion profile shapes, results in a modification to the FP. While more clusters need be studied, our work shows that broken structural homology is not solely responsible for the tilt of the FP, but allowing for variations caused by such structural differences does reduce the tilt. It is likely that the departure of the observed FP from the virial plane will be further reduced by using infrared luminosity profile measurements to

minimise stellar population effects. Our best estimate of the FP using the parameters from an $R^{1/n}$ profile and the total aperture velocity dispersion is $R \propto \sigma^{1.44 \pm 0.11} \Sigma^{-0.93 \pm 0.08}$. The exponent of the surface brightness term is consistent with the prediction of the virial theorem.

Acknowledgments

We thank Richard Bower, John Lucey, and Richard Ellis for kindly making their galaxy profile data available to us in electronic form. We are grateful for discussions with George Djorgovski, and Reinaldo de Carvalho. We also appreciate the useful suggestions and comments from Mike Pahre that helped to improve this paper. We are grateful for Luca Ciotti's suggestion to explore use of the total aperture velocity dispersion in our study. We wish to thank Eric Feigelson and Michael Akritas at the Statistical Consulting Centre for Astronomy at Pennsylvania State University, for their advice on the construction of the Fundamental Plane. We are grateful for the use of Eric Feigelson's computer code SLOPES. This research has made use of the NASA/IPAC Extragalactic Database (NED) which is operated by the Jet Propulsion Laboratory, California Institute of Technology, under contract with the National Aeronautics and Space Administration.

REFERENCES

- Aaronson M., Persson S.E., Frogel J.A., 1981, *ApJ*, 245, 18
 Andredakis Y.C., Peletier R.F., Balcells M., 1995, *MNRAS*, 275, 874
 Binggeli B., Cameron L.M., 1991, *A&A*, 252, 27
 Binney J., Tremaine S., 1987, *Galactic Dynamics*, Princeton University Press, Princeton, p.205
 Bower R.G., Lucey J.R., Ellis R.S., 1992, *MNRAS*, 254, 589
 Brosche P., Lentes F.-Th., 1983, in Athanassoula E., ed, *Proc. IAU Symp. 100, Internal Kinematics and Dynamics of Galaxies*. Reidel, Dordrecht, p.377
 Burkert A., 1993, *A&A*, 278, 23
 Burstein D., Faber S.M., Dressler A., 1990, *ApJ*, 354, 18
 Burstein D., Heiles C., 1984, *ApJS*, 54, 33
 Burstein D., Davies R.L., Dressler A., Faber S.M., Stone R.P.S., Lynden-Bell D., Terlevich R.J., Wegner G., 1987, *ApJS*, 64, 601
 Caon N., Capaccioli M., D'Onofrio M., 1993, *MNRAS*, 265, 1013
 Caon N., Capaccioli M., D'Onofrio M., Longo G., 1994, *A&A*, 286, L39
 Capaccioli M., 1987, in de Zeeuw T., ed, *Proc. IAU Symp. 127, Structure and Dynamics of Elliptical Galaxies*, Reidel, Dordrecht, p.47
 Capaccioli M., 1989, in Corwin H G., Bottinelli L., eds, *The World of Galaxies*, Springer-Verlag, Berlin, p.208
 Capelato H.V., de Carvalho R.R., Carlberg R.G., 1995, *ApJ*, 451, 525
 Ciotti L., 1991, *A&A*, 249, 99
 Ciotti L., 1994, *Cel. Mech. & Dynam. Astr.*, 60, 401
 Ciotti L., Lanzoni B., 1996, *A&A*, submitted
 Ciotti L., Lanzoni B., Renzini A., 1996, *MNRAS*, 282, 1
 Courteau S., de Jong R.S., Broeils A.H., 1996, *ApJ*, 457, L1
 Davies R.L., Burstein D., Dressler A., Faber S.M., Lynden-Bell D., Terlevich R.J., Wegner G., 1987, *ApJS*, 64, 581
 Davies J.I., Phillips S., Cawson M.G.M., Disney M.J., Kibblewhite E.J., 1988, *MNRAS*, 232, 239
 de Carvalho R.R., Djorgovski S., 1992, *ApJ*, 389, L49
 de Vaucouleurs G., 1948, *Ann d'Ap.*, 11, 247
 de Vaucouleurs G., 1953, *MNRAS*, 113, 134
 Djorgovski S., 1987a, in de Zeeuw T., ed, *Proc. IAU Symp. 127, Structure and Dynamics of Elliptical Galaxies*, Reidel, Dordrecht, p.79
 Djorgovski S., 1987b, in Thuan T.X., Montmerle T., Tran Thanh Van J., eds, *Starbursts and Galaxy Evolution*, Editions Frontieres, France, p.549
 Djorgovski S., Davis M., 1987, *ApJ*, 313, 59
 Djorgovski S., de Carvalho R., Han M.S., 1988, in Pritchet C.J., VanderBergh S., eds, *ASP Conf. Proc. 4, The Extragalactic Distance Scale*, ASP, San Francisco, p.329
 Djorgovski S., Santiago B.X., 1993, in Danziger J. et al./, eds, *Proc. of the ESO/EIPC Workshop on Structure, Dynamics, and Chemical Evolution of Early-Type Galaxies*, ESO Publication 45, p.59
 Dressler A., 1984, *ApJ*, 281, 512
 Dressler A., 1987, *ApJ*, 317, 1
 Dressler A., Faber S.M., 1990, *ApJ*, 354, 13
 Dressler A., Faber S.M., Burstein D., Davies R.L., Lynden-Bell D., Terlevich R.J., Wegner G., 1987a, *ApJ*, 313, L37
 Dressler A., Lynden-Bell D., Burstein D., Davies R.L., Faber S.M., Terlevich R.J., Wegner G., 1987b, *ApJ*, 313, 42
 Faber S.M., Jackson R., 1976, *ApJ*, 204, 668
 Faber S.M., Dressler A., Davies R.L., Burstein D., Lynden-Bell D., Terlevich R.J., Wegner G., 1987, in Faber S.M., ed, *Nearly Normal Galaxies*, Springer, New York, p.175
 Feigelson E.D., Babu G.J., 1992, *ApJ*, 397, 55
 Graham A., Lauer T.R., Colless M., Postman M., 1996, *ApJ*, 465, 534
 Guzman R., Lucey J.R., 1993, *MNRAS*, 263, L47
 Guzman R., Lucey J.R., Bower R.G., 1993, *MNRAS*, 265, 731
 Hernquist L., 1990, *ApJ*, 356, 359
 Hjorth J., Madsen J., 1991, *MNRAS*, 253, 703
 Hjorth J., Madsen J., 1995, *ApJ*, 445, 55
 Isobe T., Feigelson E.D., Akritas M.G., Babu G.J., 1990, *ApJ*, 364, 104
 Jaffe W., 1983, *MNRAS*, 202, 995
 Jarvis B.J., Peletier R.F., 1991, *A&A*, 247, 315
 Jørgensen I., Franx M., Kjaergaard P., 1996, *MNRAS*, 280, 167
 Kaiser N., 1988, in Mezzetti M., Giuricin G., Mardirossian F., Ramella M., eds, *Large-Scale Structure and motion in the Universe*, Kluwer Academic Publisher, Dordrecht, p.197
 Lynden-Bell D., Burstein D., Davies R.L., Dressler A., Faber S.M., Terlevich R., Wegner G., 1988a, in Pritchet C.J., VanderBergh S., eds, *ASP Conf. Proc. 4, The Extragalactic Distance Scale*, ASP, San Francisco, p.307
 Lynden-Bell D., Faber S.M., Burstein D., Davies R.L., Dressler A., Terlevich R., Wegner G., 1988b, *ApJ*, 326, 19
 Lucey J.R., Bower R.G., Ellis R.S., 1991, *MNRAS*, 249, 755
 Lucey J.R., Carter D., 1988, *MNRAS*, 235, 1177
 Lucey J.R., Guzman R., Carter D., Terlevich R.J., 1991, *MNRAS*, 253, 584
 McElroy D.B., 1995, *ApJS*, 100, 105
 Merritt D., 1985, *AJ*, 90, 1027
 Michard R., 1982, *A&AS*, 49, 591
 Michard R., 1985, *A&A*, 59, 205
 Murtagh F., Heck A., 1987, *Multivariate Data Analysis*, Reidel, Dordrecht
 Osipkov L.P., 1979, *Pis'ma Astron.Zh.*, 5, 77
 Pahre M.A., Djorgovski S.G., de Carvalho R.R., 1995, *ApJ*, 453, L17
 Poveda A., Iturriaga R., Orozoco I., 1960, *Bol. Obs. Tonantzintla*, No. 20, 3
 Recillas-Cruz E., Carrasco L., Serrano A.P.G., Cruz-González I., 1990, *A&A*, 229, 64
 Renzini A., Ciotti L., 1993, *ApJ*, 416, L49
 Saglia et al. 1996, preprint

- Sandage A., 1973, ApJ, 183, 711
Schombert J.M., 1986, ApJS, 60, 603
Sersic J.-L., 1968, Atlas de Galaxias Australes, Observatorio Astronomico, Cordoba
Silk J., 1989, ApJ, 345, L1
Wegner G., Saglia R.P., McMahan R.K. Jr, Davies R.L., Colless M., Burstein D., Bertschinger E., Baggley G., 1996, in preparation
Whitmore B.C., 1980, 242, 53
Worthey G., 1994, ApJS, 95, 107
Young P.J., 1976, AJ, 81, 807

Figure 1. The residual V-band aperture magnitude data (beyond 3 FWHM, and taken from Bower, Lucey & Ellis (1992)) about the best fitting $R^{1/4}$ and $R^{1/n}$ profile models is shown, being open triangles and solid squares respectively.

Figure 2. The average shape parameter n , from the $R^{1/n}$ models, is plotted against the average spatial half-mass radius for the 26 E/S0 Virgo galaxies from Bower, Lucey, & Ellis (1992).

Figure 3. The shape parameter n , from the $R^{1/n}$ models, is plotted against the projected effective radius for all the the images (including multiples). Also shown are the 1σ error ellipses, as described in the text.

Figure 4. The χ^2 value of the best fitting $R^{1/n}$ (filled square), and ($R^{1/4}$ + sky-correction) (star), model, normalised against the χ^2 value of the best fitting $R^{1/4}$ model, is plotted against n . The ratio is of course close to 1 near $n = 4$, and is smaller when away from $n=4$, indicating a superior fit of the model to the data.

Figure 5. The χ^2 value of the best fitting ($R^{1/4}$ + sky-correction) model, normalised against the χ^2 value of the best fitting $R^{1/4}$ model, is plotted against the size of the sky correction expressed as the associated change in the half-light magnitude.

Figure 6. The ratio of the χ^2 fit from the best fitting $R^{1/n}$ model to the best fitting $R^{1/4}$ model with a sky-correction, is plotted against the size of the sky correction expressed as the associated change in the half-light magnitude.

Figure 7. The spatial ($\sigma(r)$, solid), line-of-sight ($\sigma_{ls}(R)$, dashed), and aperture ($\sigma_{ap}(R)$, dotted) velocity dispersion profiles are shown for a range of shape parameters n for the $R^{1/n}$ luminosity profile. The abscissa is such that $s = r/R_e$ and $\eta = R/R_e$.

Figure 8. The ratio of the aperture velocity dispersion, as calculated in Appendix B, to the spatial half-mass velocity dispersion, as a function of projected aperture size. The abscissa is such that $\eta = R/R_e$

Figure 9. Total galaxy mass plotted against the shape parameter n .

Figure 10. a) The FP constructed using an $R^{1/4}$ law to derive the spatial half-mass radius (R) and mean surface brightness (μ); and using the central projected aperture velocity dispersion measure for σ . b) Similar to (a) except that $R^{1/n}$ profile parameters were used. c) Similar to (b) except that the spatial half-light velocity dispersion term is used instead of the central aperture velocity dispersion. d) Constructed using the parameters from an $R^{1/n}$ law and the total (infinite) aperture velocity dispersion term.

Figure 11. Ratio of the derived effective radii from the $R^{1/n}$ and the $R^{1/4}$ model is shown against the shape parameter n . A clear systematic effect of under and over estimation of the effective radius is evident when applying the $R^{1/4}$ law to large and small galaxies respectively.

Figure A1. The structural luminosity term K_L (s.t. $-2.5\log(K_L) = \langle\mu\rangle_e - \mu_e - 2.5\log(\pi)$) is plotted as a function of n , for Sersic's $R^{1/n}$ law. The dashed line aids the eye for the case where $n = 4$, giving the result for the de Vaucouleurs $R^{1/4}$ law.

APPENDIX A: DERIVATION OF $\langle\mu\rangle_E$ FROM AN $R^{1/N}$ CURVE OF GROWTH

From equation 1 the Sersic law (Sersic 1968), describing the projected light distribution for elliptical galaxies, bulges and disks is given by

$$I = I_e e^b e^{-b(R/R_e)^{1/n}}. \quad (\text{A1})$$

The average intensity, $\langle I \rangle_e$, within the effective radius, R_e , of the model is obtained from

$$\langle I \rangle_e = \frac{\int I dA}{A} = \frac{I_e e^b \int_0^{R_e} e^{-b(R/R_e)^{1/n}} 2\pi R dR}{\pi R_e^2}. \quad (\text{A2})$$

This expression can be simplified by letting $x = b(R/R_e)^{1/n}$, giving

$$\langle I \rangle_e = I_e f(n), \quad (\text{A3})$$

where

$$f(n) = \frac{2ne^b}{b^{2n}} \int_0^b e^{-x} x^{2n-1} dx. \quad (\text{A4})$$

Now as b was chosen such that R_e is the radius containing half of the total light from the galaxy, we have

$$f(n) = \frac{ne^b}{b^{2n}} \int_0^\infty e^{-x} x^{2n-1} dx = \frac{ne^b}{b^{2n}} \Gamma(2n) = \frac{k_L}{\pi}, \quad (\text{A5})$$

where k_L is the luminosity structure term mentioned in section 3.2. By taking the logarithm, we obtain

$$\langle\mu\rangle_e = \mu_e - 2.5 \log[f(n)]. \quad (\text{A6})$$

The value of μ_e comes straight from the fitted $R^{1/n}$ model, and $f(n)$ is computable and shown in Figure A1 for a range of n that covers typical observational data. This result is in agreement with the previous work of Caon et al. (1994).

APPENDIX B: VELOCITY DISPERSION PROFILES

The spatial luminosity density $\nu(r)$ can be computed from the projected luminosity profile $I(R)$ of the galaxy, such that

$$\nu(r) = \frac{-1}{\pi} \int_r^\infty \frac{dI(R)}{dR} \frac{dR}{\sqrt{R^2 - r^2}}, \quad (\text{B1})$$

where R is the projected radius and r is the spatial radius of the galaxy (Binney & Tremaine 1987).

This has been done for the $R^{1/4}$ profile (Poveda, Iturriaga & Orozoco 1960; Young 1976), and the generalisation to the $R^{1/n}$ profile (Ciotti 1991) is

$$\nu_n(s) = \frac{b^n x^{1-n}}{\pi} \int_0^1 \frac{1}{t^2} \frac{\exp(-x/t)}{\sqrt{t^{-2n} - 1}} dt, \quad (\text{B2})$$

where $s = r/R_e$ and $x = bs^{1/n}$. We have replaced the dummy variable t in Ciotti's expression by $1/t$, so as to avoid an integration to infinity. The physical value for the luminosity density is given by $\nu(r) = I_e e^b / R_e \nu(s)$. Following Ciotti's Figure 2, Figure B1 shows the luminosity density as a function of the normalised radius s , for a range of shape parameters n .

The integrated spatial luminosity is then

$$L_n(s) = 4\pi \int_0^s \nu_n(s') s'^2 ds', \quad (\text{B3})$$

and is shown in Figure B2, with n ranging from 1 to 15. Here we have that $L_n(r) = I_e e^b R_e^2 L_n(s)$, where $L_n(r)$ yields the same total luminosity as given by equation 2. We include Figures B1 and B2 in our paper for ease of reference and as they cover a greater range of shape parameters than in Ciotti's Figure 2 ($n = 2 - 10$), where we encompass the $n = 1$ model being representative of an exponential disk and all integer values up to $n = 15$ being the cut off used by Caon et al. (1993).

For a spherical galaxy, with isotropic dynamics, constant M/L , and in hydrostatic equilibrium, the Jeans hydrodynamical equation can be written as $d(\nu\sigma^2)/dr = G(M/L)L(r)\nu/r^2$. Integration with the boundary condition $\nu\sigma^2 \rightarrow 0$ as $r \rightarrow \infty$ gives

$$\sigma_n^2(s) = \frac{1}{\nu_n(s)} \int_0^{1/s} L_n(1/t) \nu_n(1/t) dt, \quad (\text{B4})$$

where we have dropped the constants $G(M/L)$. Again, we have replaced the dummy variable t with $1/t$. This expression for the velocity dispersion is dimensionless, the physical value $\sigma_n^2(r)$ being given by

$$\sigma_n^2(r) = G(M/L) I_e e^b R_e \sigma_n^2(s). \quad (\text{B5})$$

The line of sight velocity dispersion is given by Ciotti (1991) as

$$\sigma_{ls,n}^2(\eta) = -2e^{b\eta^{1/n}} \int_0^{1/\eta} L_n(1/t) \nu_n(1/t) \sqrt{1/t^2 - \eta^2} dt, \quad (\text{B6})$$

where $\eta = R/R_e$. The luminosity weighted aperture velocity dispersion is then

$$\sigma_{ap,n}^2(\eta_{ap}) = \frac{\int_0^{\eta_{ap}} I(\eta) \sigma_{ls}(\eta) \eta d\eta}{\int_0^{\eta_{ap}} I(\eta) \eta d\eta}, \quad (\text{B7})$$

Figure B1. The spatial luminosity density (ν) profiles are shown for a range in n from the exponential model, where $n = 1$, to $n = 15$, with $s = r/R_e$ being the 3D spatial radius divided by the projected half-light radius. (Extension of Fig. 2 from Ciotti (1991) which plotted values of n ranging from 2 to 10).

Figure B2. The integrated spatial luminosity, normalised by the total profile luminosity, is plotted as a function of $s = r/R_e$. (Extension of Fig. 2 from Ciotti (1991) which plotted values of n ranging from 2 to 10).

where $I(\eta)$ is the $R^{1/n}$ profile. The physical quantity $\sigma_{ap,n}^2(R_{ap})$ being given by the same transformation, such that

$$\sigma_{ap,n}^2(R_{ap}) = G(M/L) I_e e^b R_e \sigma_{ap,n}^2(\eta_{ap}). \quad (\text{B8})$$

Shown in Figure 7 are the spatial, line of sight, and aperture velocity dispersion as a function of radius for different $R^{1/n}$ profiles. It is noted that this quantity is dimensionless and should be multiplied by $G(M/L) I_e e^b R_e$ to obtain the physical quantity. The ratio of the spatial velocity dispersion at the spatial half-mass radius, $s \sim 1.34$, to the aperture velocity dispersion at the value of η corresponding to the ratio of the aperture size used and the projected half-light radius of the galaxy, can be used to correct the measured central velocity dispersion to the physical value at the spatial half-mass radius. Thus, the multiplicative factor doesn't come into play in this conversion process.

Table 1. The galaxy sample is from Bower, Lucey & Ellis (1992). Multiple observations (V-band) allow one to gauge the accuracy of the fitted model parameters due to various measurement errors and seeing conditions. Parameters from the best fitting $R^{1/4}$ and $R^{1/n}$ laws are shown. $R_{e,n}$ is the effective half-light radius and $\Sigma_{e,n}$ the mean surface brightness within this radius.

Galaxy Ident.	Obs. no.	n	Sersic law		de Vaucouleurs law ($n=4$)	
			$\log R_{e,n}$ [kpc]	$\Sigma_{e,n}$ [mag arcsec $^{-2}$]	$\log R_{e,4}$ [kpc]	$\Sigma_{e,4}$ [mag arcsec $^{-2}$]
N4339	1	4.26	0.29	20.89	0.24	20.73
	2	4.74	0.35	21.13	0.22	20.65
N4365	1	3.82	0.43	20.13	0.47	20.26
N4371	1	3.24	0.25	20.11	0.40	20.64
	2	3.10	0.20	19.96	0.39	20.62
N4374	1	3.58	0.34	19.27	0.43	19.58
N4377	1	5.35	0.12	20.10	-0.03	19.55
	2	8.30	0.46	21.43	-0.05	19.46
N4382	1	9.87	1.79	24.66	0.54	20.10
	2	9.64	1.62	24.08	0.42	19.74
N4387	1	2.36	-0.19	19.34	-0.01	19.98
	2	2.17	-0.20	19.31	-0.03	19.90
N4406	1	5.27	0.89	21.41	0.58	20.33
N4435	1	4.43	0.22	19.75	0.17	19.56
	2	3.80	0.07	19.22	0.10	19.32
N4442	1	2.77	-0.02	18.68	0.15	19.28
	2	2.96	0.00	18.73	0.16	19.33
N4458	1	5.27	0.41	21.71	0.21	20.98
	2	2.54	0.01	20.33	0.19	20.95
	3	4.09	0.18	20.88	0.16	20.83
N4464	1	2.33	-0.40	18.80	-0.38	18.80
	2	2.63	-0.41	18.72	-0.36	18.89
N4468	1	2.98	0.08	21.36	0.27	22.02
N4472	1	3.31	0.52	19.58	0.70	20.19
N4473	1	4.05	0.09	18.95	0.08	18.92
N4476	1	3.28	-0.10	19.89	-0.02	20.18
	2	3.06	-0.13	19.81	-0.03	20.19
N4478	1	1.64	-0.18	18.70	0.13	19.80
N4486	1	1.57	0.20	18.71	1.00	21.16
	2	1.54	0.19	18.69	1.01	21.17
	3	1.78	0.25	18.87	0.94	21.00
	4	1.57	0.21	18.73	0.97	21.08
	5	1.56	0.21	18.75	0.99	21.12
	6	1.55	0.19	18.69	1.07	21.30
N4486	7	1.66	0.23	18.78	1.00	21.15
	8	1.61	0.21	18.74	1.00	21.16
N4550	1	1.94	-0.14	19.07	0.11	19.94
	2	1.85	-0.16	19.02	0.17	20.19
N4551	1	2.24	-0.10	19.61	0.16	20.51
N4552	1	3.99	0.18	19.03	0.19	19.04
	2	4.12	0.22	19.17	0.20	19.10
	3	4.30	0.24	19.25	0.19	19.07
	4	5.44	0.41	19.87	0.19	19.06
	5	5.12	0.36	19.69	0.19	19.06
	6	6.46	0.56	20.43	0.20	19.08
	7	5.36	0.42	19.92	0.23	19.21
	8	5.45	0.40	19.85	0.19	19.07
	9	4.44	0.27	19.34	0.20	19.08
	10	4.96	0.32	19.53	0.18	19.01
	11	4.12	0.21	19.13	0.19	19.06
	12	5.18	0.37	19.74	0.20	19.11
	13	3.96	0.17	18.99	0.18	19.02
	14	5.70	0.43	19.95	0.18	19.05
N4564	1	3.82	0.09	19.59	0.11	19.68
	2	5.47	0.25	20.21	0.07	19.51
N4621	1	4.01	0.43	20.00	0.43	20.00
	2	5.90	0.65	20.83	0.30	19.55

Table 1. – *continued*

Galaxy Ident.	Obs. no.	n	Sersic law		de Vaucouleurs law ($n=4$)	
			$\log R_{e,n}$ [kpc]	$\Sigma_{e,n}$ [mag arcsec $^{-2}$]	$\log R_{e,4}$ [kpc]	$\Sigma_{e,4}$ [mag arcsec $^{-2}$]
N4636	1	3.63	0.57	20.61	0.66	20.93
	2	3.78	0.64	20.86	0.70	21.04
N4660	1	3.41	-0.19	18.46	-0.15	18.60
	2	3.49	-0.19	18.44	-0.15	18.58
	3	3.67	-0.19	18.44	-0.16	18.56
	4	3.54	-0.20	18.41	-0.17	18.53
N4697	1	4.64	0.72	20.76	0.58	20.26

Table 2. The galaxy sample is from Bower, Lucey & Ellis (1992). Parameters from the best fitting $R^{1/4}$ and $R^{1/n}$ profiles have been corrected to a form suitable for use in the construction of the Fundamental Plane. $R_{e,4}$ and $R_{e,n}$ are the spatial (3 dimensional) half-light radii of the $R^{1/4}$ law and the $R^{1/n}$ law respectively, with $\Sigma_{e,4}$ and $\Sigma_{e,n}$ the mean surface brightness term within R_e . σ_0 is the central aperture velocity dispersion measure. $\sigma_{1/2,4}$ and $\sigma_{1/2,n}$ are the spatial velocity dispersions at the spatial half-light radius of the $R^{1/4}$ and the $R^{1/n}$ profiles respectively (as detailed in the text), and $\sigma_{\text{tot},n}$ is the aperture velocity dispersion, for the $R^{1/n}$ model, with radius extended to infinity.

Galaxy Ident.	σ_0 km s ⁻¹	n	log $R_{e,n}$ [kpc]	$\Sigma_{e,n}$ [mag]	$\sigma_{1/2,n}$ km s ⁻¹	$\sigma_{\text{tot},n}$ km s ⁻¹	log $R_{e,4}$ [kpc]	$\Sigma_{e,4}$ [mag]	$\sigma_{1/2,4}$ km s ⁻¹
N4339	112*	4.50	0.45	21.00	79	84	0.36	20.69	83
N4365	258	3.82	0.56	20.13	188	195	0.60	20.26	185
N4371	127	3.17	0.35	20.03	100	101	0.53	20.63	92
N4374	302	3.58	0.47	19.27	227	233	0.56	19.58	217
N4377	136	6.82	0.46	20.57	83	97	0.09	19.50	107
N4382	200	9.76	1.85	24.33	72	94	0.61	19.91	143
N4387	115	2.26	-0.07	19.32	103	102	0.11	19.94	90
N4406	226	5.27	1.02	21.41	138	152	0.71	20.33	160
N4435	171	4.11	0.28	19.45	128	134	0.26	19.43	130
N4442	217	2.87	0.12	18.70	181	182	0.29	19.30	163
N4458	89	3.97	0.36	20.84	67	70	0.32	20.92	67
N4464	120	2.48	-0.28	18.76	112	111	0.24	18.84	102
N4468	74*	2.98	0.21	21.36	61	61	0.40	22.02	55
N4472	298	3.31	0.65	19.58	225	229	0.83	20.19	209
N4473	185	4.05	0.22	18.95	141	148	0.21	18.92	142
N4476	79*	3.17	0.02	19.85	67	68	0.11	20.18	62
N4478	148	1.64	-0.05	18.70	136	133	0.26	19.80	112
N4486	337	1.61	0.34	18.74	294	287	1.13	21.14	236
N4550	81*	1.89	-0.02	19.04	74	72	0.27	20.06	61
N4551	105	2.24	0.04	19.61	92	91	0.29	20.51	79
N4552	246	4.90	0.47	19.49	169	182	0.32	19.07	184
N4564	153	4.64	0.31	19.86	110	118	0.22	19.59	117
N4621	218	4.95	0.68	20.34	143	155	0.50	19.75	158
N4636	201	3.70	0.74	20.73	146	150	0.81	20.98	141
N4660	183	3.53	-0.06	18.44	153	157	0.03	18.57	148
N4697	189	4.64	0.85	20.76	124	133	0.71	20.26	133

* Corrected value taken from McElroy (1995).

Table 3. Fractional Variance from the PCA Analysis

model	Var ₁	Var ₂	Var ₃
$R^{1/4}, \sigma_0$	56.47%	42.26%	1.27%
$R^{1/n}, \sigma_0$	63.68%	35.68%	0.64%
$R^{1/n}, \sigma_{1/2,n}$	64.78%	34.40%	0.82%
$R^{1/n}, \sigma_{\text{tot},n}$	61.96%	37.30%	0.74%

Table 4. Fundamental Plane $R \propto \sigma^A \Sigma^B$ via the 3D bisector method

model	$R \propto \sigma^A \Sigma^B$		rms residual
	A	B	
$R^{1/4}, \sigma_0$	1.33 ± 0.10	-0.79 ± 0.11	0.053
$R^{1/n}, \sigma_0$	1.26 ± 0.10	-0.78 ± 0.08	0.053
$R^{1/n}, \sigma_{1/2, n}$	1.48 ± 0.13	-1.00 ± 0.09	0.062
$R^{1/n}, \sigma_{\text{tot}, n}$	1.44 ± 0.11	-0.93 ± 0.08	0.057

Table 5. Regression Analysis for $\log R_e$ versus $(\log \sigma + b\Sigma_e)$. All results are from the program SLOPES (Feigelson & Babu 1992). The reader is referred to their paper for an understanding of each method of analysis. The approach referred to as $R^{1/4}[\sigma_0]$ uses the projected half-light radius from the $R^{1/4}$ model, the mean surface-brightness within this radius and the projected central velocity dispersion in the construction of the FP. $R^{1/n}[\sigma_0]$, $R^{1/n}[\sigma_{1/2,n}]$ and $R^{1/n}[\sigma_{\text{tot},n}]$ use the spatial half-light radius from the $R^{1/n}$ model and the associated surface brightness term which allows for different luminosity structures in each galaxy as represented by n . These approaches use the projected central velocity dispersion term, the spatial half-light velocity dispersion term and the infinite aperture velocity dispersion term respectively.

method	Asymptotic Formulae Slope (A)	Bootstrap Slope (A)	Jackknife Slope (A)
$R^{1/4}[\sigma_0] : b = 0.236 \pm 0.031$			
OLS(Y X)	1.256±0.080	1.257±0.088	1.256±0.088
OLS(X Y)	1.377±0.067	1.384±0.076	1.378±0.079
OLS bisector	1.315±0.069	1.318±0.077	1.315±0.077
Orthogonal	1.332±0.070	1.336±0.080	1.332±0.079
Reduced major axis	1.315±0.069	1.319±0.077	1.315±0.077
Mean OLS	1.317±0.068	1.321±0.076	1.317±0.077
$R^{1/n}[\sigma_0] : b = 0.254 \pm 0.027$			
OLS(Y X)	1.200±0.050	1.198±0.064	1.200±0.058
OLS(X Y)	1.249±0.044	1.256±0.057	1.250±0.052
OLS bisector	1.224±0.045	1.226±0.058	1.224±0.049
Orthogonal	1.229±0.045	1.232±0.059	1.230±0.050
Reduced major axis	1.224±0.045	1.226±0.058	1.225±0.049
Mean OLS	1.225±0.045	1.227±0.058	1.225±0.049
$R^{1/n}[\sigma_{1/2,n}] : b = 0.285 \pm 0.032$			
OLS(Y X)	1.347±0.073	1.332±0.090	1.346±0.100
OLS(X Y)	1.439±0.054	1.442±0.071	1.439±0.058
OLS bisector	1.392±0.059	1.385±0.074	1.391±0.072
Orthogonal	1.407±0.058	1.403±0.075	1.407±0.067
Reduced major axis	1.392±0.059	1.386±0.074	1.392±0.072
Mean OLS	1.393±0.059	1.387±0.073	1.392±0.071
$R^{1/n}[\sigma_{\text{tot},n}] : b = 0.270 \pm 0.029$			
OLS(Y X)	1.333±0.067	1.324±0.083	1.333±0.086
OLS(X Y)	1.408±0.053	1.413±0.068	1.409±0.058
OLS bisector	1.370±0.057	1.367±0.071	1.370±0.065
Orthogonal	1.382±0.056	1.381±0.072	1.382±0.062
Reduced major axis	1.370±0.057	1.368±0.071	1.370±0.065
Mean OLS	1.371±0.056	1.369±0.071	1.371±0.064